AGU PUBLICATIONS

JGR

Journal of Geophysical Research: Atmospheres

RESEARCH ARTICLE
10.1002/2013JD020914

Key Points:
- Tropospheric and stratospheric ozone from Aura OMI/MLS
- Tropospheric ozone dynamics and chemistry
- Stratospheric ozone dynamics and chemistry

Correspondence to:
J. R. Ziemke,
jerald.r.ziemke@gsfc.nasa.gov

Citation:
Ziemke, J. R., et al. (2014), Assessment and applications of NASA ozone data products derived from Aura OMI/MLS satellite measurements in context of the GMI chemical transport model, *J. Geophys. Res. Atmos.*, *119*, 5671–5699, doi:10.1002/2013JD020914.

Received 27 SEP 2013
Accepted 10 APR 2014
Accepted article online 14 APR 2014
Published online 13 MAY 2014

Assessment and applications of NASA ozone data products derived from Aura OMI/MLS satellite measurements in context of the GMI chemical transport model

J. R. Ziemke[1,2], M. A. Olsen[1,2], J. C. Witte[3], A. R. Douglass[2], S. E. Strahan[2,4], K. Wargan[2,3], X. Liu[5], M. R. Schoeberl[6], K. Yang[7], T. B. Kaplan[8], S. Pawson[2], B. N. Duncan[2], P. A. Newman[2], P. K. Bhartia[2], and M. K. Heney[3]

[1]Goddard Earth Sciences Technology and Research, Morgan State University, Baltimore, Maryland, USA, [2]Goddard Space Flight Center, NASA, Greenbelt, Maryland, USA, [3]Science Systems and Applications, Inc., Lanham, Maryland, USA, [4]Universities Space Research Association, Columbia, Maryland, USA, [5]Harvard-Smithsonian Center for Astrophysics, Cambridge, Massachusetts, USA, [6]Science and Technology Corporation, Lanham, Maryland, USA, [7]Department of Atmospheric and Oceanic Science, University of Maryland, College Park, Maryland, USA, [8]INNOVIM, Greenbelt, Maryland, USA

Abstract Measurements from the Ozone Monitoring Instrument (OMI) and Microwave Limb Sounder (MLS), both on board the Aura spacecraft, have been used to produce daily global maps of column and profile ozone since August 2004. Here we compare and evaluate three strategies to obtain daily maps of tropospheric and stratospheric ozone from OMI and MLS measurements: trajectory mapping, direct profile retrieval, and data assimilation. Evaluation is based on an assessment that includes validation using ozonesondes and comparisons with the Global Modeling Initiative (GMI) chemical transport model. We investigate applications of the three ozone data products from near-decadal and interannual time scales to day-to-day case studies. Interannual changes in zonal mean tropospheric ozone from all of the products in any latitude range are of the order 1–2 Dobson units while changes (increases) over the 8 year Aura record investigated vary by 2–4 Dobson units. It is demonstrated that all of the ozone products can measure and monitor exceptional tropospheric ozone events including major forest fire and pollution transport events. Stratospheric ozone during the Aura record has several anomalous interannual events including split stratospheric warmings in the Northern Hemisphere extratropics that are well captured using the data assimilation ozone profile product. Data assimilation with continuous daily global coverage and vertical ozone profile information is the best of the three strategies at generating a global tropospheric and stratospheric ozone product for science applications.

1. Introduction

There are several different methods for deriving both column ozone and profile ozone from satellite. Subtraction of stratospheric column ozone (SCO) from total ozone column, known as the tropospheric ozone residual method [*Fishman et al.*, 1990], yields a quantitative measure of tropospheric column ozone (TCO). The original application of the method subtracted SCO obtained from Stratospheric Aerosol and Gas Experiment (SAGE) profiles from colocated Total Ozone Mapping Spectrometer (TOMS) total column ozone. This residual concept has also been used with TOMS total ozone and SCO from solar backscatter ultraviolet (SBUV) instruments [*Fishman et al.*, 2003] and from the Upper Atmosphere Research Satellite Microwave Limb Sounder (MLS) instrument [*Chandra et al.*, 2003]. Other methods to derive TCO from satellite measurements include a modified residual method incorporating TOMS-only total ozone [*Hudson and Thompson*, 1998], a UV radiance scan angle method [*Kim et al.*, 2001], a topography differencing method [*Newchurch et al.*, 2001], and cloud slicing using deep convective clouds [*Ziemke et al.*, 1998, 2009]. These techniques produce tropospheric ozone fields that have limited temporal or spatial coverage.

Our study focuses on ozone products derived from the Aura Ozone Monitoring Instrument (OMI) and Microwave Limb Sounder (MLS). These two instruments are currently operating, and their measurements are being used in several new algorithms for deriving tropospheric and stratospheric ozone, both in column amounts and profiles. While the MLS instrument remains fully functional for measuring ozone and other trace

gases, the OMI measurements are impacted by a "row anomaly" artifact which has adversely affected between one third to one half of the ozone measurements since 2009 [e.g., *Yan et al*., 2012]. The OMI row anomaly is caused by physical material which has become dislodged and is blocking the optical path.

Liu et al. [2010a, 2010b] uses an optimal estimation technique to determine ozone profiles from OMI radiances. This is a direct profile retrieval method using a single instrument and gives both stratospheric and tropospheric column ozone once the tropopause is specified. The row anomaly adversely affected profiles after January 2009. Therefore, our study uses only ozone profiles through December 2008. We also evaluate fields produced by data assimilation of OMI and MLS ozone measurements (K. Wargan et al., The global structure of ozone in the UTLS region in an assimilation of EOS-Aura data, manuscript in preparation, 2014). The third product uses a trajectory mapping technique [*Schoeberl et al*., 2007] that estimates SCO fields by advecting MLS profile ozone using analyzed winds and filling in subsequent SCO measurements between Aura orbits. TCO then follows from the trajectory mapping method by subtracting SCO from OMI total column ozone. *Schoeberl et al*. [2007] show that use of trajectory mapping to fill in regions between MLS tracks improves both daily TCO and SCO measurements beyond the Gaussian/linear interpolation method of *Ziemke et al*. [2006]. The assimilation and trajectory techniques both invoke MLS measurements that have better vertical profile resolution near the tropopause (~3 km) for separating tropospheric from stratospheric ozone compared to direct nadir profile retrieval (~7–11 km).

The main purpose of our study is to assess data quality and science application capability of these three gridded OMI/MLS ozone products. Assessment of the products includes comparisons with ozonesondes and ozone simulated using the Global Modeling Initiative (GMI) chemistry and transport model (CTM) as well as evaluation of the suitability of these products for science applications. The following sections 2 and 3 describe the data sets used and the GMI CTM. Section 4 provides a brief description of the three ozone data products evaluated in our study. Section 5 shows ozonesonde comparisons for validation of the products, while section 6 discusses fundamental seasonal and spatial characteristics for these products. Section 7 describes applications for the products, and finally, section 8 provides a summary.

2. Description of Relevant Data Sets

Ozone data from Aura OMI and MLS instruments are used to create daily maps of tropospheric column ozone (TCO) and profile ozone. The OMI and MLS ozone data are available as level-2 (along-orbit swath) and level-3 (gridded for OMI) beginning in late August 2004. The Aura OMI is a nadir-scanning instrument. At visible and UV wavelengths OMI detects backscattered solar radiance to measure daytime total column ozone over the Earth with a resolution of 13 km × 24 km at absolute nadir. Documentation for the OMI instrument and data may be obtained from the webpage http://eospso.gsfc.nasa.gov/atbd-category/49. Our analyses use OMI version 8.5 ozone measurements which include several changes from version 8 including measured cloud pressures [*Vasilkov et al*., 2008]. The sensitivity of the OMI total ozone algorithm to ozone varies spatially due to changes in surface reflectivity and also varies strongly with altitude. Retrieval efficiency, i.e., approximately the ability in percent to detect ozone from backscattered radiation, on average varies from ~100% in the stratosphere and upper troposphere to 40–70% at 3 km. The use of OMI spectra with additional wavelengths in the direct ozone profile retrieval slightly increases the retrieval efficiency in the lower troposphere [*Liu et al*., 2010a]. The OMI instrument cannot detect ozone lying below thick clouds, so to estimate the total ozone column in the atmosphere the OMI retrieval places a climatological "ghost column" below the clouds.

The Aura MLS instrument looks through the atmospheric limb along the orbital track and obtains a vertical ozone profile by scanning the field of view up and down. An MLS profile is obtained about 7 min before OMI for ascending orbit daytime measurements from MLS. This measurement time difference occurs because MLS looks forward along the orbital path while OMI looks down. Because MLS detects microwave emission, this instrument measures ozone profiles during both daytime (ascending orbit) and nighttime (descending orbit). All of the ozone products which use MLS data include both day and night v3.3 measurements. Data quality and description of the MLS version 3.3 ozone profile product are discussed by *Livesey et al*. [2011]. Extensive details for v3.3 ozone can be obtained also from the online data quality and description document (http://mls.jpl.nasa.gov/data/v3-3_data_quality_document.pdf).

Ozonesonde measurements are used for validation of the tropospheric ozone data products. This validation includes ozonesonde profile measurements from the World Ozone and Ultraviolet Radiation Data Centre

(WOUDC), Southern Hemisphere Additional Ozonesondes (SHADOZ), and Network for the Detection of Atmospheric Composition Change (NDACC). For consistency the tropopause pressure obtained from the World Meteorological Organization (WMO) 2 K km^{-1} vertical lapse rate definition is applied for determining TCO and SCO for all of the products including ozonesondes.

3. Description of the GMI Model

The CTM includes a photochemical mechanism for the stratosphere and troposphere and is described by *Strahan et al*. [2007] and *Duncan et al*. [2008]. The emission sources include industry/fossil fuel, biomass burning, biofuel combustions, and contributions from aircraft exhaust. The biomass burning emissions are described by *van der Werf et al*. [2006]. All global emissions for year 2004 through year 2008 for the CTM are monthly means. Global emissions in the model for year 2008 are repeated for each of the following years 2009–2012. The meteorological input fields for the model are from Modern Era Retrospective analysis for Research and Applications (MERRA).

4. Description of the Ozone Data Products

4.1. Trajectory Mapping

Schoeberl et al. [2007] describe a trajectory algorithm for producing high horizontal resolution maps of stratospheric and tropospheric column ozone. With this method the along-track profile v3.3 ozone from MLS each day is advected 2 days forward and 2 days backward to produce fields of stratospheric ozone profiles. These daily ozone profiles are then vertically integrated to produce high-resolution (1° × 1.25°) gridded maps of SCO. (The current TRAJ data product includes gridded SCO but does not include gridded stratospheric ozone profiles.) The gridded SCO is then subtracted from coincident total column ozone from OMI to produce daily global maps of TCO. This method produces daily global maps that include regions associated with the jet streams. Vertical resolution of MLS retrieved ozone in the vicinity of the tropopause is about 3 km which may impact the accuracy of derived tropospheric and stratospheric column ozone amounts by several Dobson units (DU). The speed for the trajectory algorithm is fast when compared to direct profile retrieval (section 4.2) or data assimilation methods (section 4.3). The fields produced using this method incorporate MERRA assimilated winds, the same winds as used by the CTM described in section 3. We have improved several aspects of the trajectory mapping product compared with the original product of *Schoeberl et al*. [2007]. The current version corrects a tropopause pressure error, a time stamp error affecting daily time iteration steps, and flags bad retrieval measurements for high-resolution mode days. (The high-resolution days occur about 1 day out of every 32 days on average with horizontal resolution of 6 km × 12 km at nadir). Each of these changes represents several DU improvements in the new product.

4.2. Nadir Profile

This method is based on the OMI instrument measurements alone. In the OMI ozone profile algorithm the profile of partial ozone columns in Dobson unit (DU) is retrieved at 24 layers from the surface to ~60 km (~2.5 km thick per layer) from backscattered ultraviolet radiances in the spectral region 270–330 nm using the optimal estimation technique [*Liu et al*., 2010a, 2010b]. This retrieval scheme approaches an optimal solution by simultaneously and iteratively minimizing the differences between measured and calculated theoretical radiances and between retrieved and a priori state vectors, constrained by measurement error and the monthly and zonal mean Labow-Logan-McPeters ozone profile climatology [*McPeters et al*., 2007]. The ozone profiles in the retrieval have four to seven layers in the troposphere depending on the latitude (although there are between one and two actual profile information components in the troposphere). The tropopause is used as one of the retrieval levels in the vertical grid, so stratospheric and tropospheric ozone columns can be easily integrated from the retrieved ozone profile. (Every retrieved profile has a unique set of retrieval pressures.) The horizontal resolution of our retrievals used here is 52 × 48 km^2 at nadir by coadding 4 UV1 (8 UV2) pixels. The vertical resolution, estimated by *Liu et al*. [2010a], varies from 7 to 11 km in the troposphere and 10 to 14 km in the stratosphere. The retrieval errors (defined as the root-sum-square of precisions and smoothing errors) range from 1–6% in the stratosphere to 6–35% in the troposphere. The retrieval errors in tropospheric ozone columns are typically within 2–4 DU. For this study we use the daily data gridded to 2.5° longitude × 2° latitude. Due to the occurrence of OMI row anomaly, only retrievals from October 2004 through the end of 2008 are used in this study.

4.3. Data Assimilation

The Global Modeling and Assimilation Office (GMAO) assimilated ozone product is generated by ingesting OMI v8.5 total column ozone and MLS v3.3 ozone profiles into the Goddard Earth Observing System version 5.7.2 (GEOS-5.7.2) assimilation system with several modifications listed below. GEOS-5.7.2 is an updated version of the global data assimilation system used to produce NASA's Modern Era Retrospective Analysis (MERRA reanalysis) and described by *Rienecker et al*. [2011]. It consists of an Atmospheric General Circulation Model (AGCM) and a statistical analysis module that combines 6-hourly meteorological and chemical forecasts from the AGCM with observational data from meteorology and satellite-borne sounders to produce an analysis state. The assimilation system does not include ozonesonde measurements. The AGCM is a version of the Fortuna general circulation model described in *Molod et al*. [2012]. The statistical analysis is done using the Gridpoint Statistical Interpolation (GSI) approach [*Wu et al*., 2002; *Purser et al*., 2003a, 2003b]. The assimilated product was generated at a horizontal resolution of 2° latitude by 2.5° longitude and at 72 vertical layers between the surface and 0.01 hPa. Depending on the height of the tropopause, about 25 to 35 of those layers are in the troposphere.

Ozone profiles from the MLS retrievals are given on 38 levels between 261 hPa and 0.0215 hPa. Prior to assimilation each profile is averaged in the vertical, so that the midlevel average values of the mixing ratios are assimilated. The "midlevel" is the log-pressure center point between two consecutive MLS levels while the midlevel mixing ratio is obtained by taking the arithmetic average of mixing ratio from these two surfaces in log pressure. The averaging improves the precision of mixing ratio values while preserving the integrated columns. In order to account for variable sensitivity in the vertical of total ozone measurements by the OMI instrument, we use the efficiency factor information (averaging kernels) provided with the data to weight the impact of these observations in the vertical. The GSI convolves the forecast ozone profile at each OMI observation location and the climatological a priori with their respective efficiency factors and subtracts their sum from the observed value of the total ozone column. By doing this, the dependence on OMIs a priori is largely removed in the assimilation. Although the row anomaly has time dependence that affects a growing number of rows over the Aura record, the assimilation uses the same OMI level-2 rows #2–24 over the entire record for consistency. The GEOS-5 AGCM transports the assimilated ozone using the assimilated meteorology, but complete ozone chemistry is not accounted for. There is no model chemistry in the troposphere, and only a dry deposition mechanism at the surface is applied. This approach works well because the ozone time scale is long compared to the 6 h between analysis times when the background field is corrected by observations. In the stratosphere the model applies time-dependent (monthly) zonally symmetric ozone production and loss rates derived from a two-dimensional model as in *Stajner et al*. [2008]. This approach also works well for the same reason of comparatively long ozone lifetimes in the lower stratosphere which contributes the bulk of the total ozone column.

The main differences between the operational configuration of GEOS-5.7.2 and the system used in this study are (1) the use of MLS ozone data instead of solar backscatter ultraviolet observations, (2) the use of efficiency factors for OMI, (3) state-dependent background error covariances similar to those used in *Stajner et al*. [2008], and (4) the absence of an ozone chemistry parameterization below the tropopause. A complete description of this system is given by K. Wargan et al. (manuscript in preparation, 2013). Ozonesonde validation of the assimilated ozone profiles is shown by K. Wargan et al. (manuscript in preparation, 2013) and primarily focuses on the variability and structure of ozone in the upper troposphere and lower stratosphere. Information that data assimilation has of tropospheric ozone comes from OMI total column ozone which has reduced sensitivity in the low troposphere as mentioned in section 2.

5. Ozonesonde Validation of the TCO Products

Ozonesonde measurements are used to evaluate the TCO gridded products at the sonde station locations shown in Figure 1. Ozonesonde profiles were integrated from ground to the tropopause to derive daily TCO measurements that were then plotted against daily TCO from the three global data products and the CTM simulation. For the remainder of our study these are abbreviated in figures and text as TRAJ, PROF, ASSIM, and GMI (corresponding to trajectory mapping, nadir profile retrieval, GMAO data assimilation, and the CTM, respectively).

Figure 2 shows TCO for the three data products and CTM plotted versus ozonesonde TCO where all days of the years (years indicated in figure caption), and all latitudes for the sondes are included. For consistency all

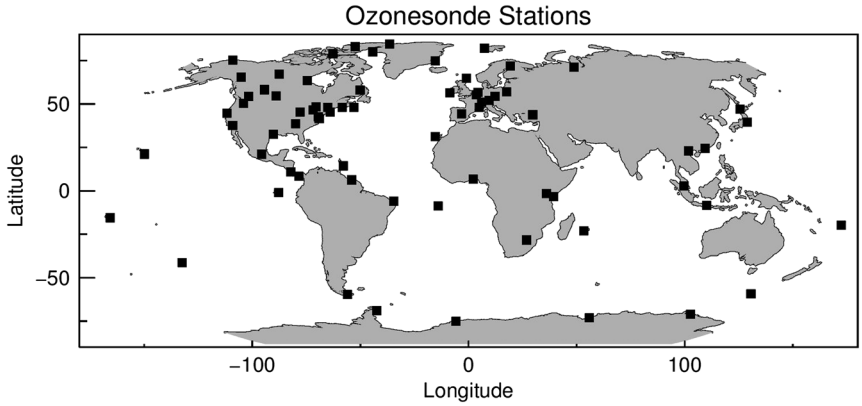

Figure 1. Geolocation sites for ozonesondes used in our study for validation of the ozone products. The ozonesonde data are daily ozone profile measurements from SHADOZ, WOUDC, and NDACC.

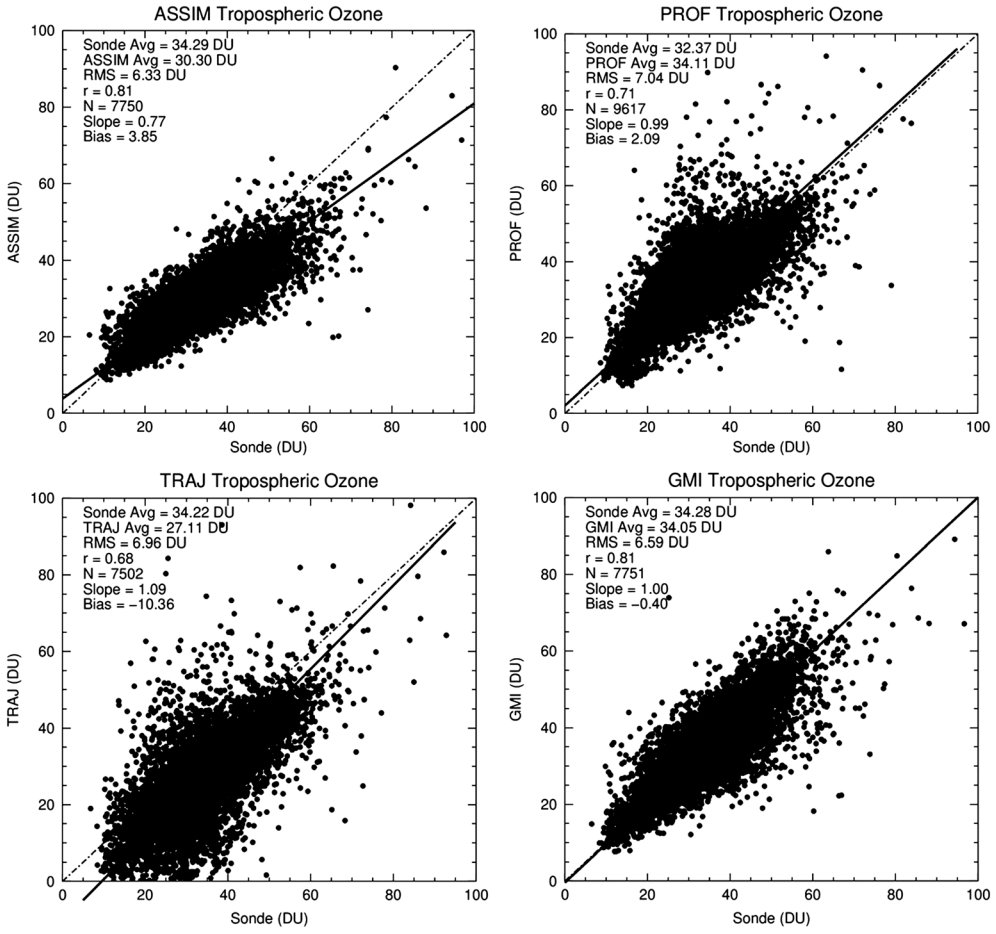

Figure 2. Daily TCO for the four products (data assimilation, direct profile retrieval, trajectory mapping, and GMI model) plotted versus coincident ozonesonde TCO. Included for each product in the scatterplots are averages, RMS value, correlation, and total number of data pairs. The 1-1 line (dot-dash line) is plotted along with the line regression fit from the data points (solid line). The listed bias in the panels is equivalent to the vertical line intercept from the regression. The years included for ozonesonde comparisons for PROF are 2004–2008 and 2005–2010 for GMI, TRAJ, and ASSIM.

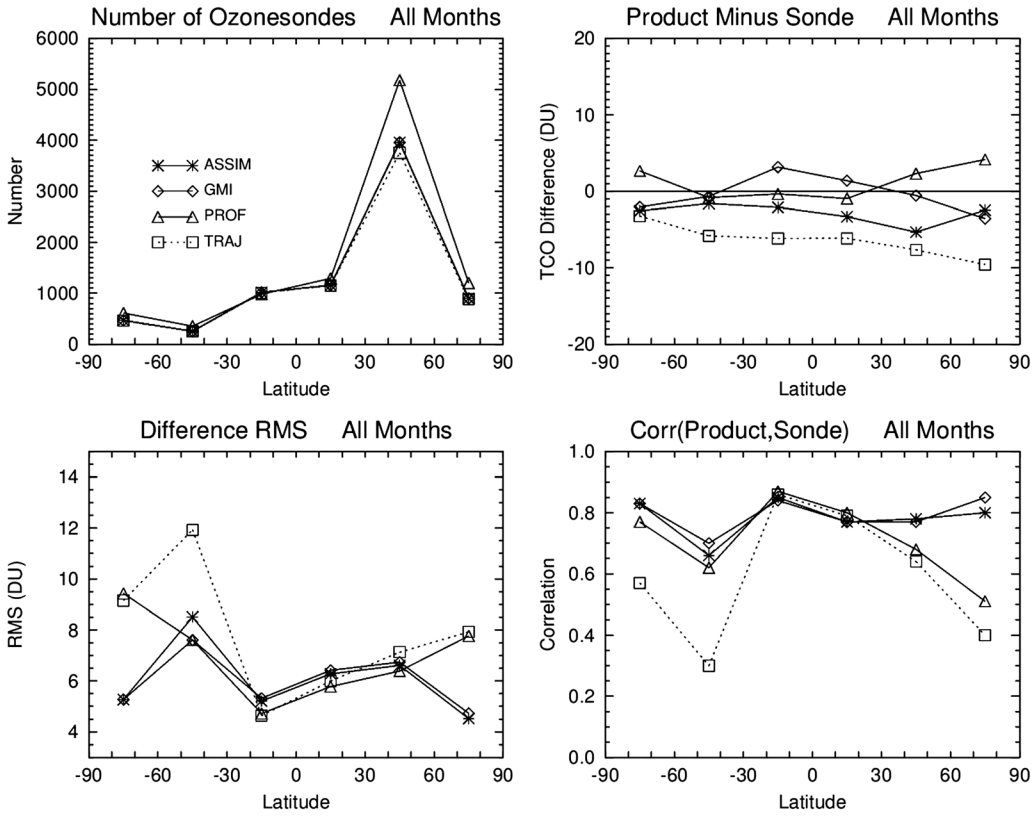

Figure 3. Expansion of the ozonesonde TCO comparisons of Figure 2 as function of latitude band for ASSIM, GMI, PROF, and TRAJ. The latitude bands are in 30° segments as follows: 60°S–90°S, 30°S–60°S, 0–30°S, 0–30°N, 30°N–60°N, and 60°N–90°N. (top left) Number of sonde measurements. (top right) Product/model minus sonde mean offset. (bottom left) Difference RMS with sondes. (bottom right) Correlation with sondes.

products and the CTM invoke the same tropopause pressures defined using the WMO 2 K km^{-1} definition. The tropopause pressures include quality flagging which filters out highly dynamical conditions such as tropopause folds which can produce large uncertainties in the derived column amounts. For the TRAJ TCO product an additional filter is applied for clouds (i.e., only OMI scenes with reflectivity less than 0.3 are used) to nearly eliminate (down to ~1–2 DU) artificial ghost column ozone in TCO. For the PROF TCO product the National Centers for Environmental Prediction (NCEP) tropopause pressures were not filtered for either clouds or highly dynamical conditions. For these reasons the values for N in Figure 2 for the three data products are all different but are similar between the CTM and ASSIM.

In Figure 2 the variability for both product and sonde comes largely from seasonal cycles as well as variations with latitude/region for the many station locations included for each scatterplot. Statistical quantities listed in each of the four scatterplots include averages (i.e., from which mean offsets are derived) and RMS differences. Time averages were removed from all data products/GMI and ozonesondes prior to calculating RMS differences. Based on Figure 2 the CTM tropospheric ozone seems to perform better than the products, but that is not the case regarding stratospheric ozone (discussed in section 7.3).

In Figure 3 the statistical analyses of Figure 2 are partitioned into six separate 30° latitude bands (indicated) to investigate hemisphere/latitude dependence. Figure 3 (top left) plots the number of coincident sonde profiles, while Figure 3 (top right, bottom left, and bottom right) shows the mean product minus sonde differences, RMS differences, and correlations with the sondes, respectively. TCO for ASSIM, GMI, PROF, and TRAJ are indicated in this figure by asterisks, diamonds, triangles, and squares, respectively. In Figure 3 the number of sondes is largest by far in the Northern Hemisphere (NH) midlatitudes, while the number in the Southern Hemisphere (SH) ranges from only a few hundreds to about 1000. Even with only 200 coincident sonde measurements, correlations greater than 0.2 exceed the 99% confidence level based on the standard two-sided *t* test for correlation [e.g., *Hogg and Craig*, 1978]. The product minus sonde TCO differences in

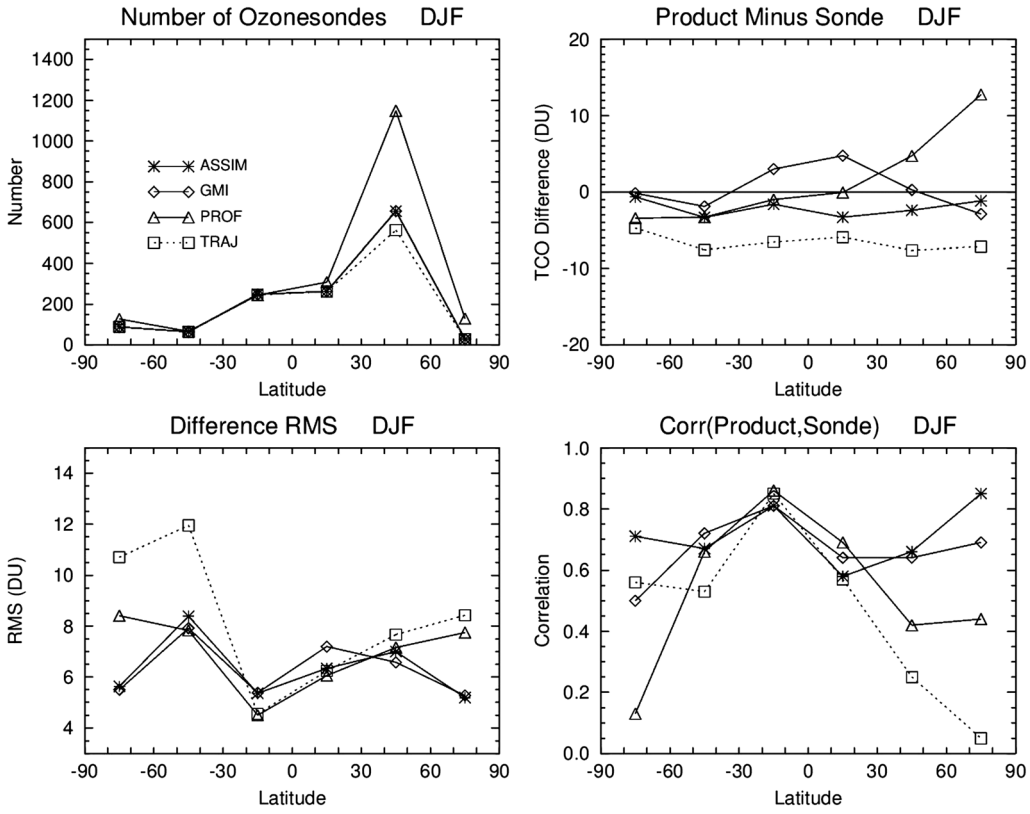

Figure 4. Same as Figure 3 but instead for only the months of December-January-February (DJF).

Figure 3 (top right) vary in latitude by only a few DUs for the CTM and products but with TRAJ ozone having largest offsets with the sondes of 5–10 DU in both hemispheres. RMS differences in Figure 3 (bottom left) vary substantially between CTM and the three products in the southern midlatitudes and both polar regions. However, RMS differences for ASSIM and the CTM are nearly the same for all latitude bands, and between 30°S and 60°N where most of the sonde measurements are made, RMS differences for all four are nearly identical with values of 5–7 DU. Correlations in Figure 3 (bottom right) are all nearly the same for 30°S to 30°N while outside this latitude range the correlation for TRAJ is lower than all the others with PROF ozone also having reduced correlations in the NH extratropics. We conclude from Figure 3 that ASSIM and CTM tropospheric ozone compare best overall with the ozonesondes based on this all-season analysis.

In Figures 4–7 we extend the statistical comparisons in Figure 3 to include seasonal dependence involving 3 month partitions of December-January-February (DJF), March-April-May (MAM), June-July-August (JJA), and September-October-November (SON). In Figures 4–7 most sonde measurements by far lie in the NH midlatitudes during JJA than for any other region and season. The number of sonde measurements for ASSIM (asterisks) and the CTM (diamonds) are essentially equivalent for all seasons and latitude ranges. For the solstice seasons of DJF (Figure 4) and JJA (Figure 6) the differences with sondes are similar to previous Figure 3 (all seasons together) but with one exception: PROF ozone has offsets greater than 10 DU during winter in both hemispheres when solar zenith angles are largest for OMI. The RMS differences for DJF (Figure 4) and JJA (Figure 6) are similar to the all-season analysis in Figure 3 for the CTM and products. The large spread of RMS difference curves in the SH for the CTM and products during both DJF and JJA coincides with a small number of sondes when compared to the NH. The sonde correlations (Figures 4 (bottom right) and 6 (bottom right)) for TRAJ are smallest compared to ASSIM, PROF, and CTM, with PROF also more weakly correlated in the winter extratropics of both hemispheres. For TRAJ TCO the sonde correlations for the SH midlatitudes in JJA and NH polar region in DJF are not statistically significant at 95% confidence level. Lastly, we compare sonde statistics for the equinox seasons of MAM (Figure 5) and SON (Figure 7). For these equinox seasons the basic characteristics noted from Figure 3 for all seasons together are similar for number of sondes, sonde difference, RMS difference, and correlation.

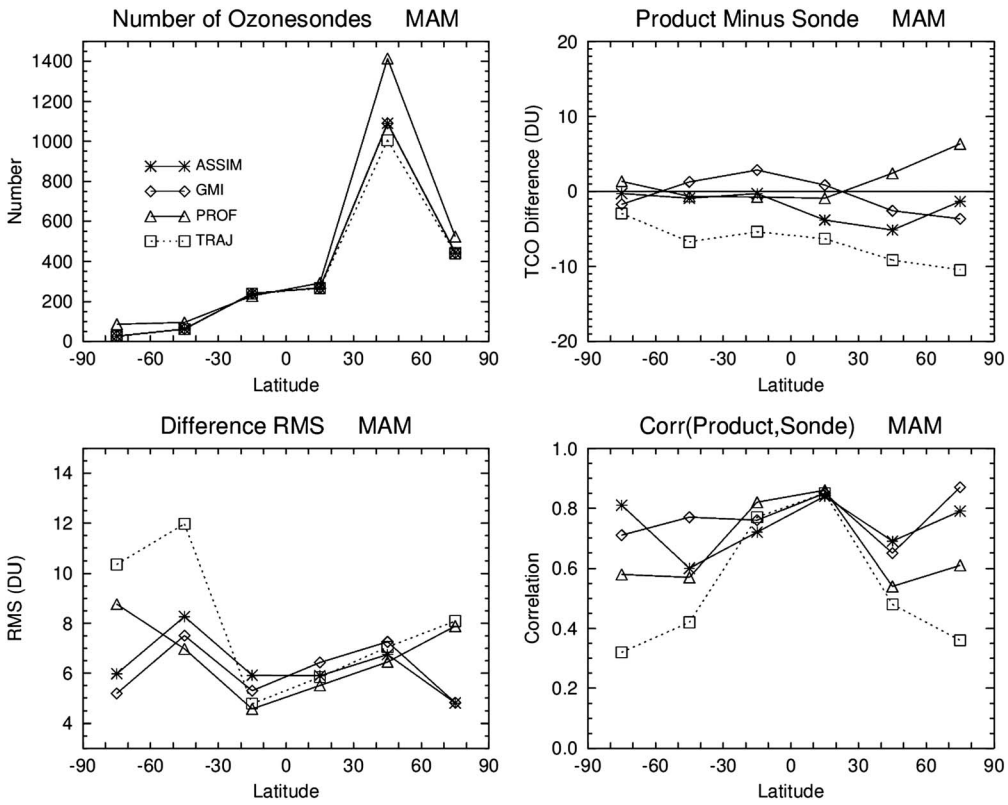

Figure 5. Same as Figure 3 but instead for only the months of March-April-May (MAM).

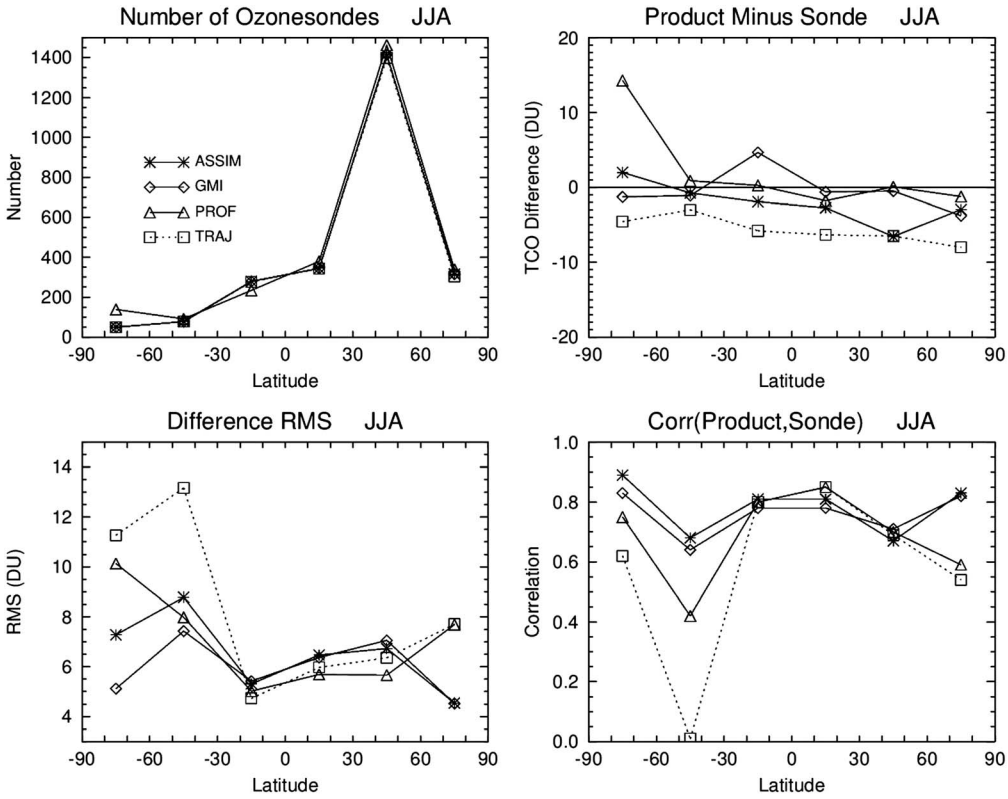

Figure 6. Same as Figure 3 but instead for only the months of June-July-August (JJA).

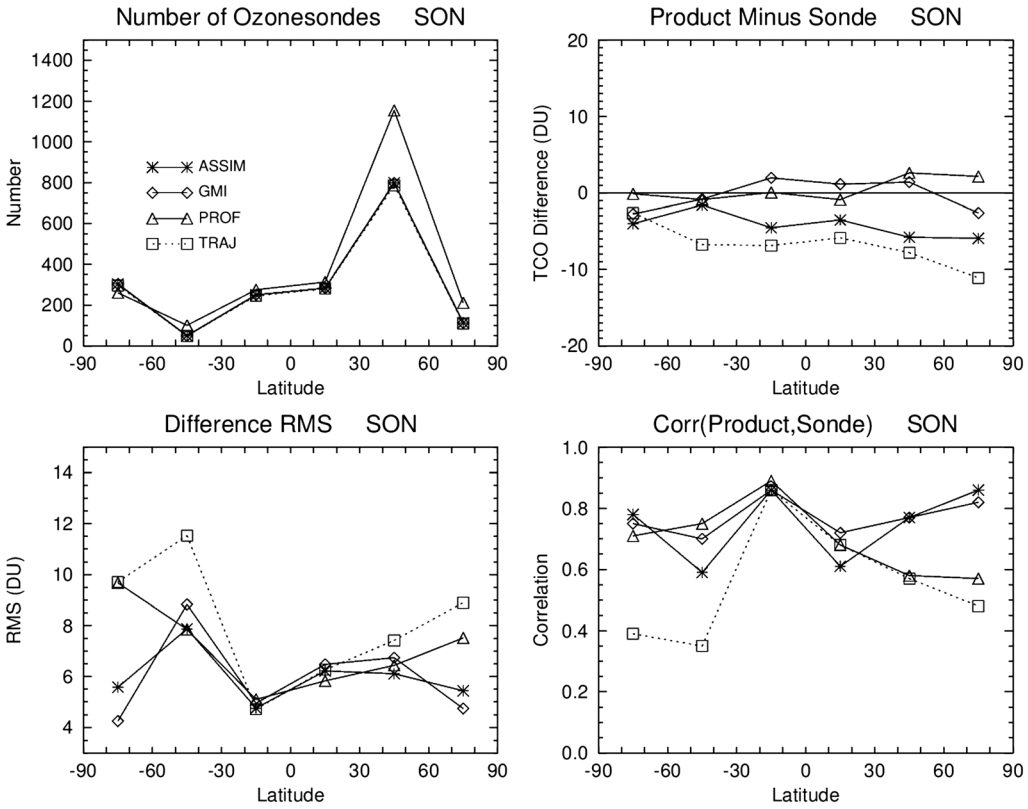

Figure 7. Same as Figure 3 but instead for only the months of September-October-November (SON).

The main conclusions that we draw from the sonde evaluations in Figures 3–7 are (1) the ASSIM TCO as a data product compares best overall with the ozonesondes, (2) comparisons for the CTM ozone and ASSIM ozone are remarkably similar, (3) PROF ozone compares about as well as both ASSIM and CTM everywhere except in the polar regions where large RMS differences and reduced correlations occur in all seasons, (4) the TRAJ ozone comparisons are the least favorable overall with similar problems in polar regions as PROF and also further discrepancies during midlatitude winter as well as a persistent offset present in all latitude ranges. As inferred from point (2) the CTM tropospheric ozone compares as well or better to sonde ozone columns as the TCO products, but as we will show in section 7.3 that the CTM unlike the products does not correctly capture stratospheric ozone variability due largely to errors in MERRA winds (an example shown is the tropical quasi-biennial oscillation (QBO)).

Although the ozonesondes are useful for validating the TCO products we can also obtain estimated uncertainties using calculated accuracy and precision. Accuracy and precision are ideally determined by extensive analysis of the various measurement errors associated with the instrument and algorithm invoked. Because of large uncertainties often present in determining these errors a common practice is to instead compare the measurements with other independent measurements of good quality (such as ozonesondes). Accuracy of the TCO products can be estimated from the ozonesonde differences in Figures 2–7. For the TRAJ and ASSIM products which both combine OMI and MLS measurements, we can estimate an upper bound for the precision of TCO. *McPeters et al*. [2008] discuss validation of the OMI daily total ozone by comparing OMI with Brewer and Dobson ground-based measurements and also with aircraft total ozone for four campaign missions. The Brewer and Dobson measurements indicated about +0.4% offset for OMI total ozone (OMI being higher), while the aircraft measurements indicated −0.2% offset with an RMS difference of 3%. Assuming average OMI total ozone of 300 DU, these numbers indicate a small offset of ~1 DU and RMS difference of 9 DU. For MLS v3.3 SCO the estimated precision is about 2% (http://mls.jpl.nasa.gov/data/v3-3_data_quality_document.pdf).

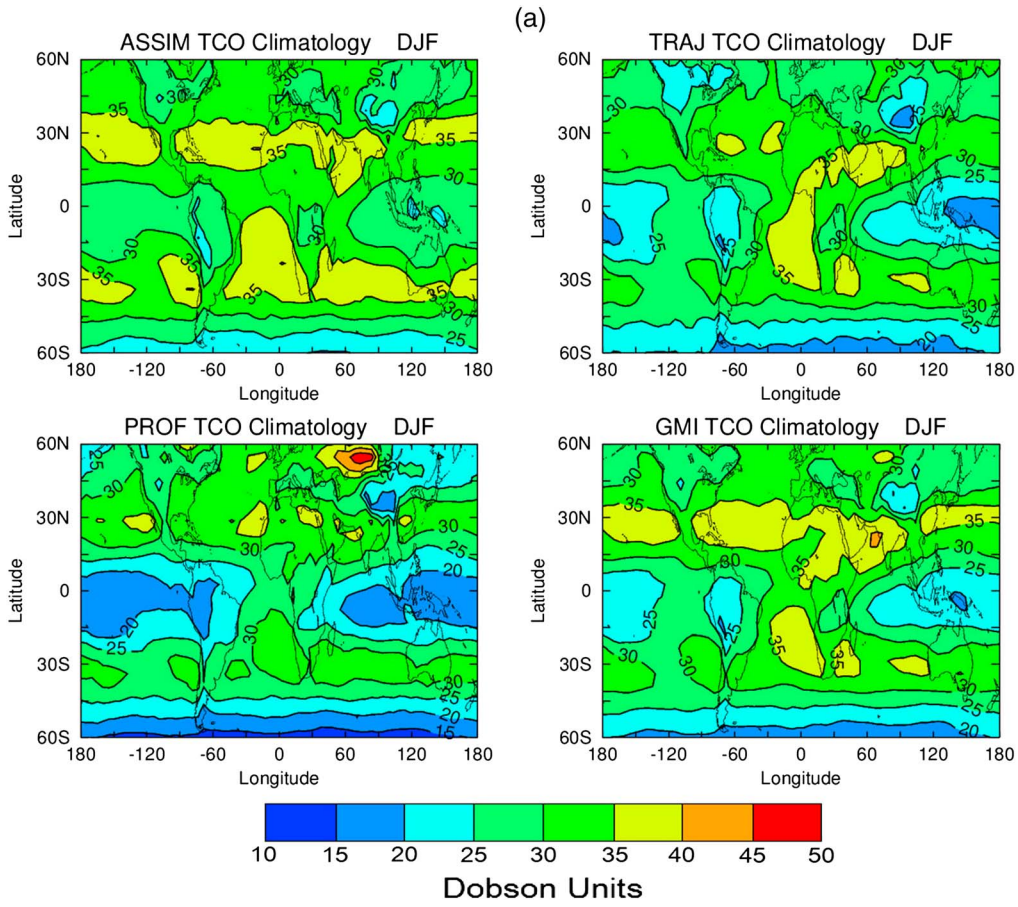

Figure 8. (a) Seasonal climatology of TCO (in Dobson units) for the December–February season for each of the three products and GMI model (indicated). (b) Similar to Figure 8a but for SCO. For this visualization comparison of spatial variability a constant offset of +4 DU, +7 DU, −2 DU, and 0 DU (based on ozonesonde differences in Figure 2) was applied to all TCO measurements for ASSIM, TRAJ, PROF, and GMI, respectively. These constant offsets were applied only for plotting TCO here and were not applied to the products in calculating the spatial statistics listed in Tables 1–3.

Assuming an average value for SCO of 270 DU, this would correspond to a precision of 5.4 DU. It follows that RMS uncertainty for TCO is given by the square root of the sum of squares of these numbers for OMI and MLS, namely, about 10.5 DU. For the PROF ozone product the precision and precision + smoothing errors (i.e., due to a priori and coarse resolution) are included for each retrieval. For PROF SCO the precision is 1–3 DU with precision + smoothing errors of 2–5 DU for solar zenith angles less than 80°. For PROF TCO the precision is 2–4 DU with precision + smoothing 2–6 DU for solar zenith angles less than 80°.

6. Spatial Variability of the Ozone Products

We next examine spatial characteristics of TCO and SCO for the three data products and CTM as functions of season to identify similarities and differences between them. Seasonal mean maps of TCO and SCO for the products and CTM are plotted in Figures 8–11 where TCO and SCO in each figure are shown as part (a) and part (b), respectively. These seasonal averages were obtained from 8 year time series (January 2005–December 2012) except for PROF measurements that extend about 4 years from October 2004 through December 2008. In our discussions and figures we refer to both as climatology even though true climatology generally refers to averaging longer-time records. Both TCO and SCO seasonal maps in Figures 8–11 can be compared directly with similar maps shown from earlier studies that also combined OMI and MLS [e.g., *Ziemke et al.*, 2011] or instead used TOMS, SAGE, and SBUV satellite measurements [e.g., *Fishman et al.*, 1990; *Wozniak et al.*, 2005].

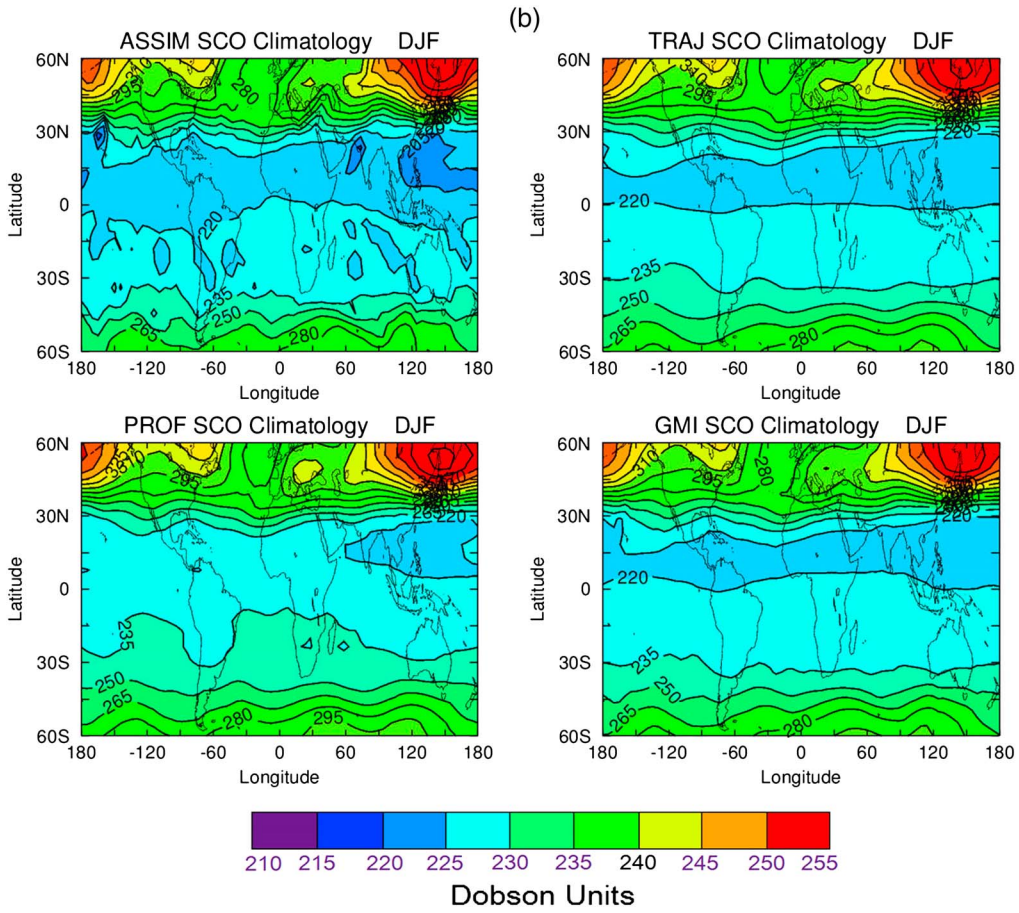

Figure 8. (continued)

We begin by discussing the TCO maps in Figures 8–11. In the tropics, TCO for the data products and the CTM in Figure 8 for DJF show a characteristic zonal wave-one variability with largest ozone in the Atlantic and smallest ozone over Indonesia. This zonal wave-one pattern in tropical TCO was first shown by *Fishman et al.* [1990] from combined TOMS and SAGE satellite measurements. The wave-one pattern occurs in all seasons with each product and the CTM as evident from Figures 9–11. For ASSIM TCO the Pacific values are larger and zonal amplitude of the wave-one pattern is smaller when compared to the other measurements and CTM. Persistence of the wave-one is due to the year-round east-west tropical Walker circulation in the troposphere. TCO in the tropics maximizes in the Atlantic region during the SON season corresponding to peak biomass burning in tropical South America and Africa. Despite this intense biomass burning, *Sauvage et al.* [2007] suggests that the annual average production of tropospheric ozone in the tropics is dominated by lightning.

All three products and CTM have smallest global mean TCO during DJF (Figure 8a). In MAM (Figure 9) TCO for all four have similar NH springtime buildup and horizontal structures. By JJA (Figure 10) all products and the CTM have largest TCO in the NH extratropics with a corresponding enhancement of TCO in the tropical/subtropical South Atlantic. The large TCO in the NH extratropics during JJA and enhanced TCO in the tropical South Atlantic in all seasons are caused by combination of many factors including stratosphere-troposphere exchange, anthropogenic pollution, and lightning as ascribed by many previous studies using both models and measurements [e.g., *Wang et al.*, 1998; *Moxim and Levy*, 2000; *Lelieveld and Dentener*, 2000; *Martin et al.*, 2003; *Chandra et al.*, 2003; *Edwards et al.*, 2003]. Spatial variability and seasonal dependence of TCO over the course of the year are almost identical, in general, sense between the three data products and CTM. During DJF TCO in the SH polar region is as small as in the tropical western Pacific.

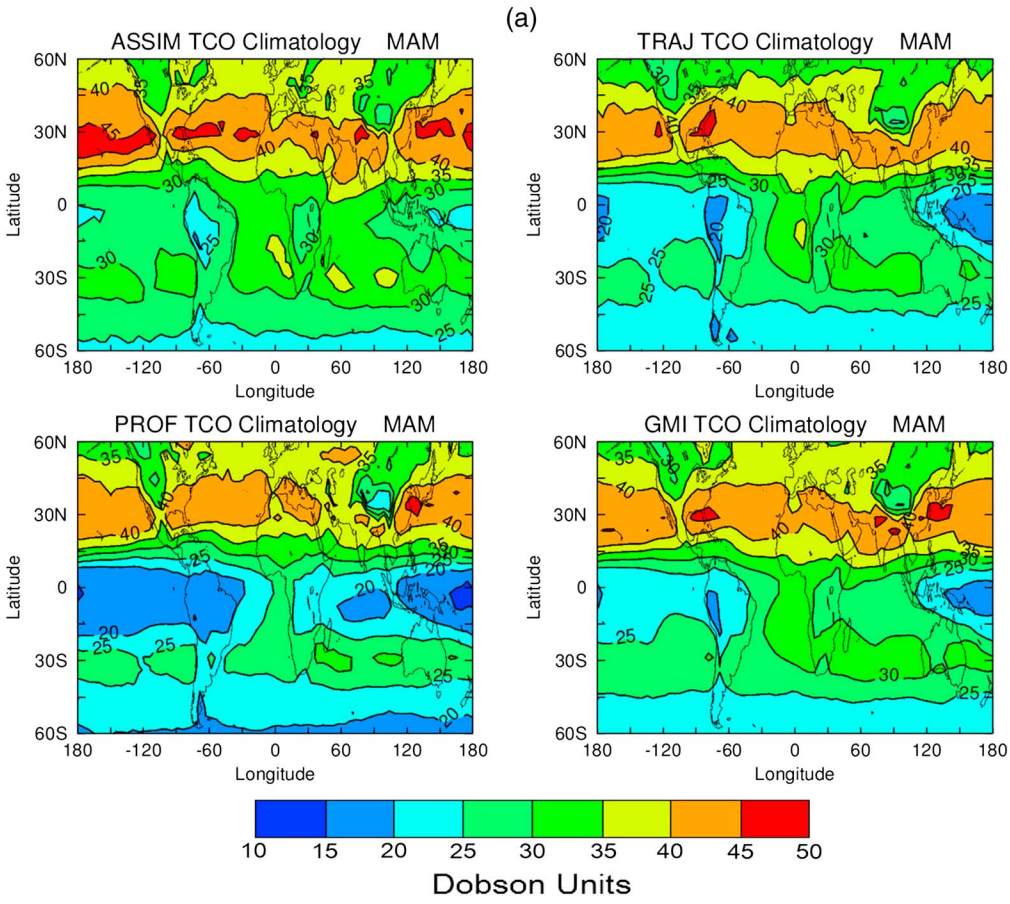

Figure 9. Similar to Figure 8 but instead for March–May season.

We next discuss the SCO maps in Figures 8–11. SCO for all three data products and CTM in each season have small spatial variability in the tropics but large spatial variability and highest column amounts in the middle-high latitudes in both hemispheres during winter-spring months. SCO during SON with all three products and CTM depict buildup of stratospheric ozone south of Australia lying northward along the edge of the SH stratospheric polar vortex. The characteristics of SCO as a function of season in Figures 8–11 can be compared with similar SCO seasonal mean maps from *Fishman et al*. [1990] using SAGE I + II ozone and from *Wozniak et al*. [2005] using both SAGE II measurements and an empirically corrected SBUV (EC-SBUV) product. Figures 6 and 7 of *Wozniak et al*. [2005] show SAGE II and EC-SBUV seasonal mean maps (DJF, MAM, JJA, and SON) from 1985 to 2000 measurements. Their SCO maps are essentially identical between SAGE II and EC-SBUV and are consistent in seasonal distribution with our Figures 8–11. Their SCO maps also indicate small spatial variability of SCO in the tropics, and numbers are mostly the same everywhere as in our Figures 8–11 except for an apparent larger abundance by about 5–10 DU in the tropics; this may be associated with the stratospheric ozone QBO and the averaging of different numbers of years.

Although TCO and SCO in Figures 8–11 from the CTM and products have similar geophysical features during all seasons there are important differences. It was noted for Figures 8–11 that TCO for all products in the tropics has a characteristic zonal wave-one pattern while SCO in the tropics exhibits small zonal variability. In Figure 12 we show TCO for the four products along the equator (Figure 12a) and corresponding SCO along the equator (Figure 12b) as month versus longitude. TCO in Figure 12a for all data products and CTM has a similar wave-one pattern that maximizes around September–October corresponding to the months of peak biomass burning over Africa and South America. The wave-one pattern of TCO for ASSIM is weaker by several DUs when compared with the other two data products and the CTM.

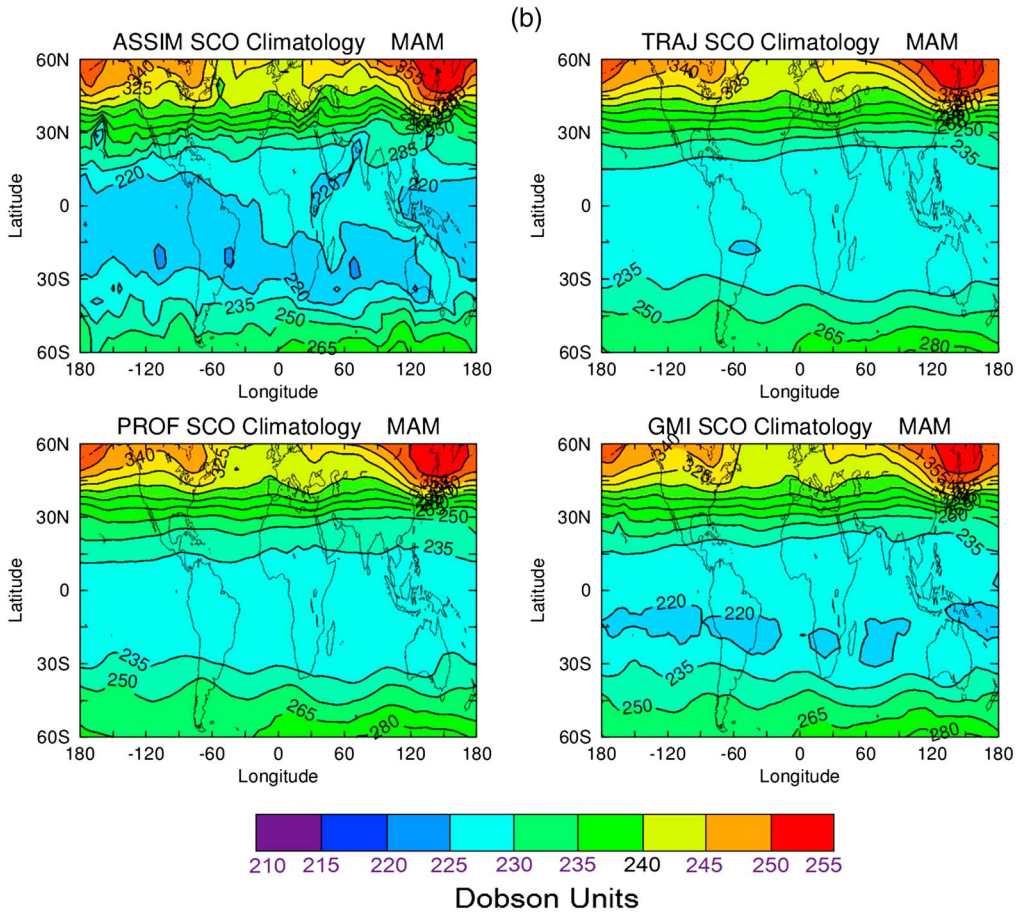

Figure 9. (continued)

For SCO there are differences in Figure 12b between the three products and CTM. TRAJ SCO in Figure 12b during any month has small zonal variability of only a few DUs. This small zonal variability of SCO has been shown in previous studies using measurements from MLS, SAGE, and Halogen Occultation Experiment satellite instruments [e.g., *Fishman et al.*, 1990; *Ziemke et al.*, 1998; *Wozniak et al.*, 2005], as well as ozonesondes [*Thompson et al.*, 2003]. SCO in Figure 12b for September (i.e., when largest SCO occurs) has zonal variability of ~10 DU for both the CTM and ASSIM, whereas zonal variability of SCO for PROF is ~5 DU and only about 2–3 DU for TRAJ. We conclude from Figure 12 that the TRAJ product is more in line with previous studies for resolving the small zonal variability of tropical SCO compared to the other data products and CTM. Since ASSIM, TRAJ, and the CTM all use essentially the same winds, this is not expected and appears to be related to vertical motion included in the CTM and ASSIM which is not included with TRAJ (e.g., TRAJ instead uses diabatic heating rates).

We include a statistical evaluation of the spatial (latitude-longitude) variability of the three TCO products ASSIM, TRAJ, and PROF. This evaluation is listed in Tables 1–3 where a subjective baseline reference TCO field for each of the four seasons was calculated by averaging corresponding seasonal means of the three data products and CTM from Figures 8–11. Spatial correlations, offsets, and RMS differences are listed in Tables 1–3 for the three data products relative to the baseline measurements. These statistical calculations for each season and each latitude band are based on 432 latitude-longitude grid points at $5° \times 5°$ resolution for all three products and CTM. The positive correlations > 0.9 in Table 1 suggest similar spatial variability, but there are also smaller correlations for both TRAJ and PROF products in the latitude bands 30°N–60°N and 30°S–60°S during winter. The mean offsets listed in Table 2 are for the most part self-explanatory with largest offsets for TRAJ followed secondly by ASSIM. The spatial RMS

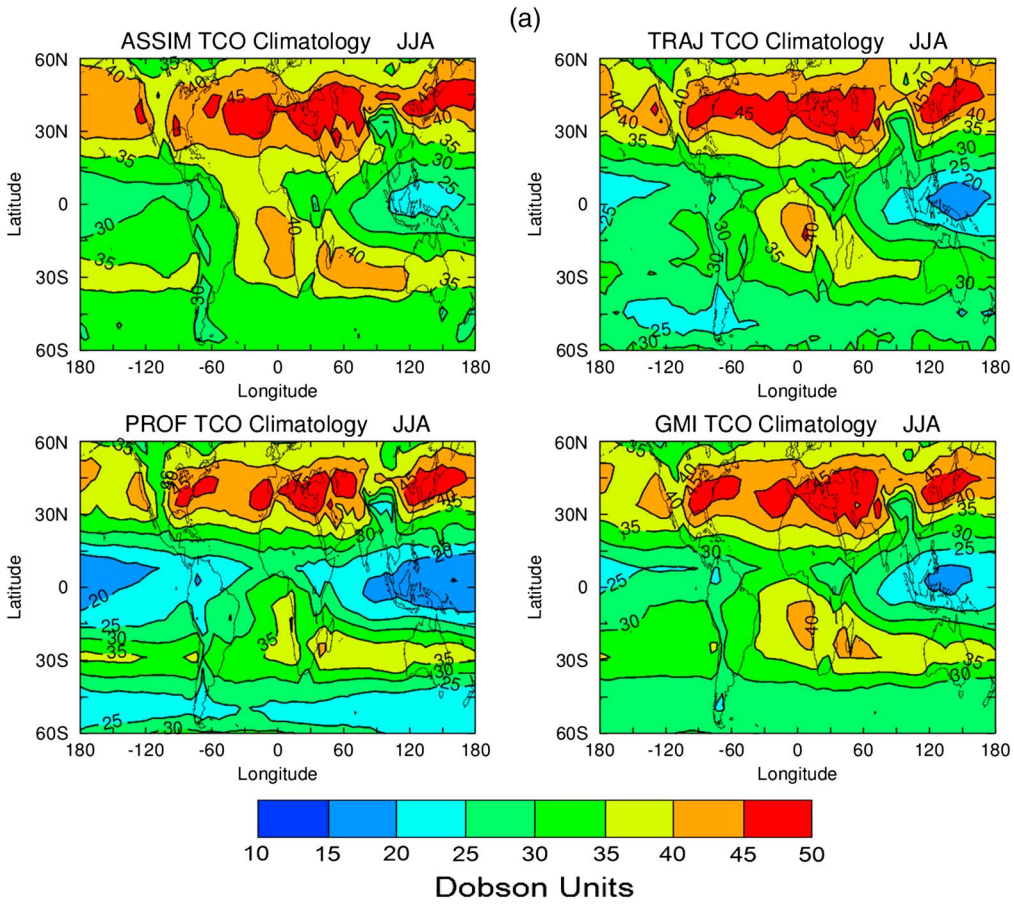

Figure 10. Similar to Figure 8 but instead for June–August season.

calculations for the data products in Table 3 are on average only about 1–2 DU. These low RMS numbers show that the three data products have similar zonal and meridional variations of TCO during all seasons and in all latitude bands.

7. Applications Using the Ozone Products

The primary ozone product which we focus on for applications is ASSIM as this product compares well with ozonesondes, has daily global coverage of long record, and provides ozone profile information (e.g., K. Wargan et al., manuscript in preparation, 2013). The TRAJ daily product does not provide ozone profile information, and the PROF daily ozone profile product extends only through year 2008 with coarse vertical resolution when compared with ASSIM. We discuss some applications in this section using these ozone products involving case studies and interannual variability.

7.1. Western Russia Wildfires of Year 2010 and Pollution Events

Record heat occurred over a broad region of Western Russia in the summer of 2010 along with related intense uncontrolled wildfires. A prolonged anticyclonic circulation over Western Russia caused sustained hot and dry conditions beginning in May 2010 and extending into early August 2010. This unusual meteorology created conditions favorable for wildfires. The breadth and intensity of the wildfires were the largest since Aura instruments began observations in the second half of 2004 [*Witte et al.*, 2011].

Figure 13a plots monthly mean TCO for ASSIM, TRAJ, and CTM for the burning region in Western Russia over the 8 year record. Peak levels of ozone are observed in July 2010 for the two data products and the CTM. In Figure 13b daily ozone profiles from ASSIM averaged over this region are plotted as log-pressure altitude

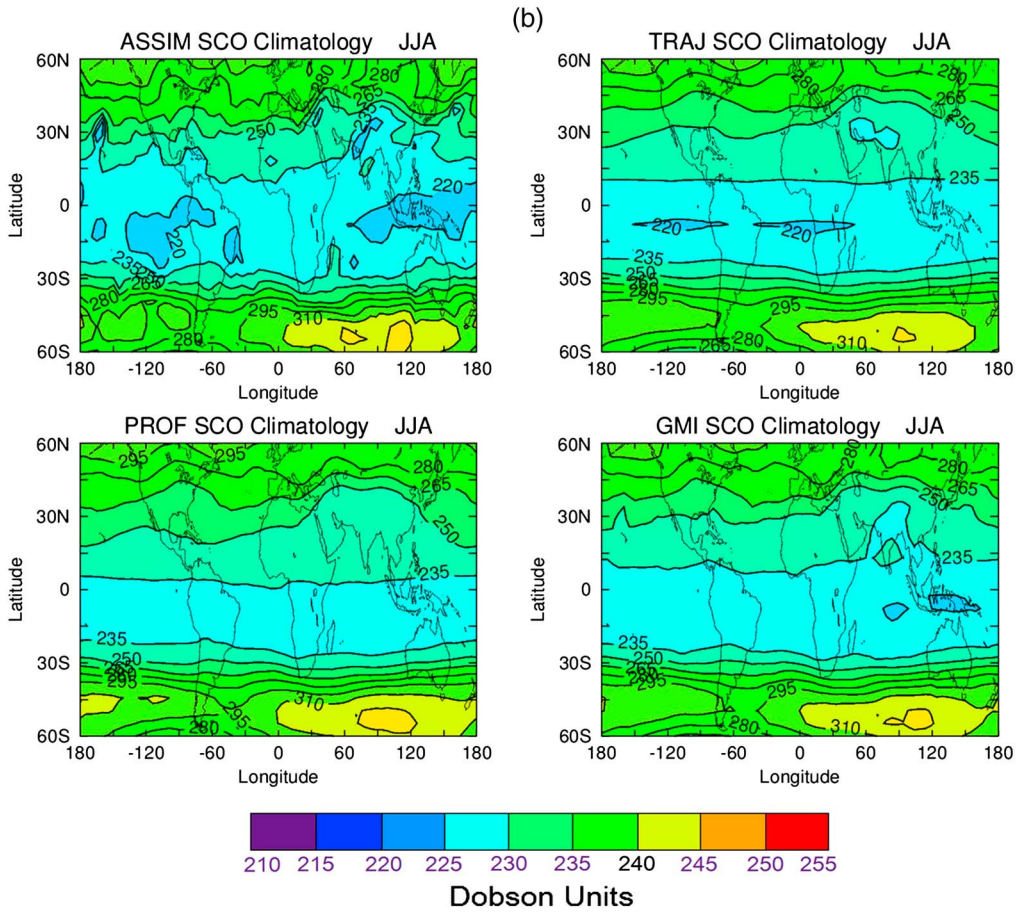

Figure 10. (continued)

versus day for year 2010. The ozone profiles in Figure 13 are given as vertical column densities (in units DU km^{-1}) to indicate relative contribution to TCO as function of altitude. The ASSIM profile ozone suggests that the anomalous increase in TCO in July 2010 extended throughout the troposphere with most contribution coming from below ~6 km. This vertical distribution of tropospheric ozone in July coincided with the anticyclonic blocking high observed by *Witte et al.* [2011] that extended from the near surface through the free troposphere.

Simulated increases in tropospheric ozone during the 2010 wildfire event suggest that anomalous meteorology is the main driver of these ozone enhancements. As described in section 3 the annual emissions for the CTM for years 2009–2012 are a repeat of the 2008 emissions and therefore the July 2010 enhanced TCO for the model in Figure 13 cannot be attributed directly to a change in emissions. *Witte et al.* [2011] showed from satellite outgoing longwave radiation (OLR) anomalously high tropospheric temperatures during summer 2010 over Western Russia compared to previous years 2003–2009. This suggests that the summer 2010 meteorology contributes to these increases in troposphere ozone. The anomalous warming in summer 2010 was associated with a persistent subsidence in the region and associated anticyclonic circulation.

Kar et al. [2010] showed that OMI/MLS tropospheric ozone has signatures of pollution in urban areas. However, while some urban regions showed local enhancement of tropospheric ozone, other urban regions did not. One important issue with detecting urban pollution ozone from OMI is that ozone sensitivity in the troposphere (which varies greatly with surface reflectivity conditions) decreases on average from about 100% in the middle-upper troposphere down to about 40%–70% at 3 km altitude and to only a few percent (if not 0 %) at the surface. Unless pollution-related ozone in the boundary

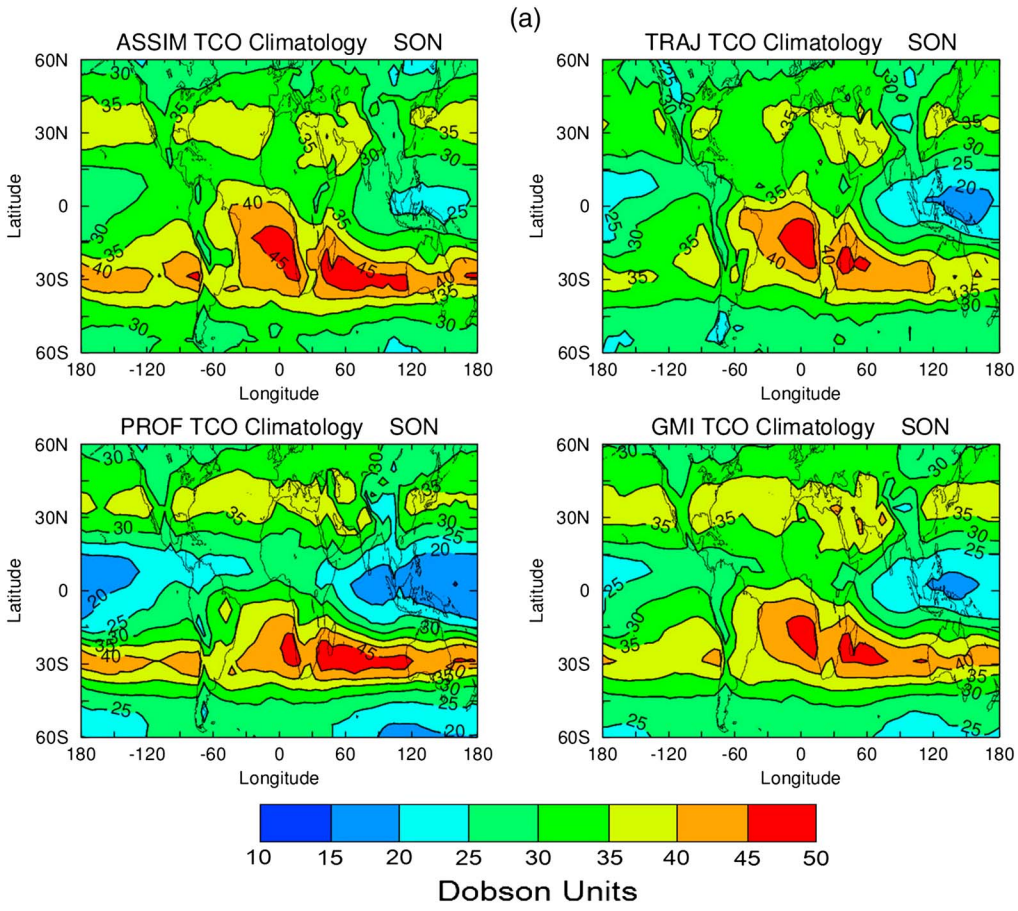

Figure 11. Similar to Figure 8 but instead for September–November season.

layer is lifted upward, it will not be readily detected by OMI. It is well known that photochemical production of ozone in the troposphere requires sufficient concentrations of NO_x and volatile organic compounds, sufficient UV radiation, and favorable meteorological conditions. Even drastic changes in pollution and ozone precursors may not significantly change tropospheric ozone. *Witte et al.* [2009] showed from OMI measurements that large reductions in tropospheric NO_2 and SO_2 occurred during the 2008 Olympics event compared to previous Aura years 2004–2007. These sharp reductions were indicative of the rigorous pollution control measures implemented over Eastern China prior to and during the Olympics. Despite the large reductions in certain target pollutants, we have found no significant reductions in TCO over Eastern China for either the TRAJ and ASSIM data products or CTM (figures not shown). It is possible that this lack of detection of ozone change may be due to the reduced OMI retrieval sensitivity in the lowermost troposphere.

We conclude that the daily ozone products can contribute to case studies involving events such as the Russian fires and the 2008 Olympics. However, much of tropospheric ozone variability occurs over longer time scales including annual cycles and interannual periods. In the following we use the important property of long decadal records with the OMI/MLS products to show applications involving interannual variability.

7.2. The Tropical El Niño Southern Oscillation

The tropical El Niño–Southern Oscillation (ENSO) is the dominant source of interannual changes of the tropical lower atmosphere and ocean. A description and historical account of ENSO is given by *Trenberth* [1997, and references therein]. "ENSO" refers to either El Niño (anomalously warm ocean temperatures in the tropical eastern Pacific) or La Niña (anomalously cool ocean temperatures in the tropical eastern Pacific).

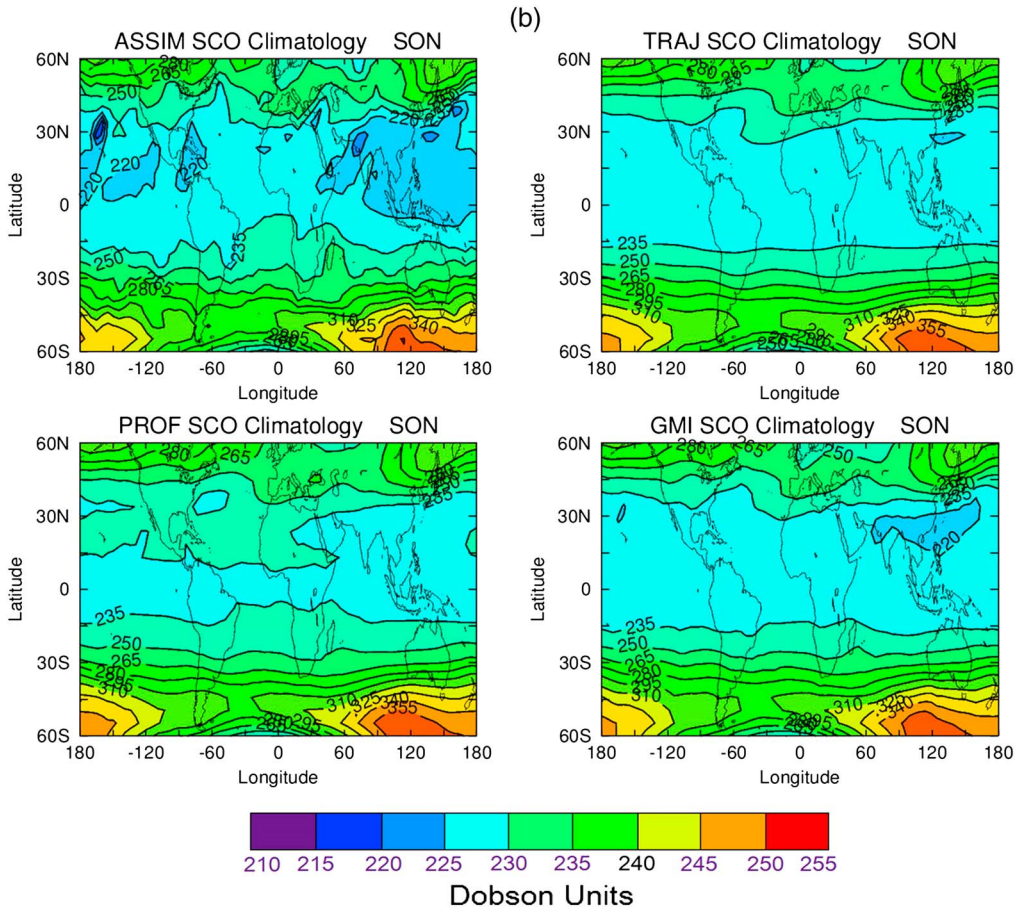

Figure 11. (continued)

Consecutive El Niño or La Niña events have a varying periodicity of about 2–7 years and usually maximize of greatest intensity during months around NH late autumn to late winter. As described by *Trenberth* [1997] there are many ENSO indices used for monitoring ENSO events, and one of the oldest indices is the Tahiti minus Darwin sea surface pressure difference known as the Southern Oscillation Index which provides a long record beginning in the 1880s. For our study we invoke the Niño 3.4 monthly ENSO index (also discussed by *Trenberth* [1997]) for comparing with ENSO-related changes in tropospheric ozone. The Niño 3.4 ENSO index is derived from sea surface temperature anomalies in the tropical eastern Pacific.

It is well known that ENSO events induce large interannual changes in tropospheric ozone in the tropical Pacific [e.g., *Chandra et al.*, 1998; *Sudo and Takahashi*, 2001; *Thompson et al.*, 2001; *Fishman et al.*, 2005; *Oman et al.*, 2013]. The most influential case was the El Niño of 1997–1998 which was associated with +20 DU to +25 DU increases in TCO in the tropical western Pacific due to combined effects from reduced convection and enhanced biomass burning in Indonesia [*Chandra et al.*, 2002]. ENSO events induce the largest interannual changes in tropical tropospheric ozone, but there is also evidence of a weak QBO signal in tropical tropospheric ozone as inferred from both satellite and SHADOZ ozonesondes [e.g., *Ziemke and Chandra*, 1999; *Chandra et al.*, 2002; *Fishman et al.*, 2005; *Lee et al.*, 2010]. The detected QBO signals in TCO appear to be only a few DUs compared to generally much larger episodic ENSO-induced variability.

A multidecadal monthly tropospheric ozone ENSO index (OEI) was derived by *Ziemke et al.* [2010] to monitor the intensity of ENSO events in tropospheric ozone and to use as a diagnostic test for models of atmospheric chemistry and transport. To calculate the OEI, TCO for each month is first averaged over the eastern Pacific (15°S–15°N, 110°W–180°) and western Pacific (15°S–15°N, 70°E–140°E). (These two regions

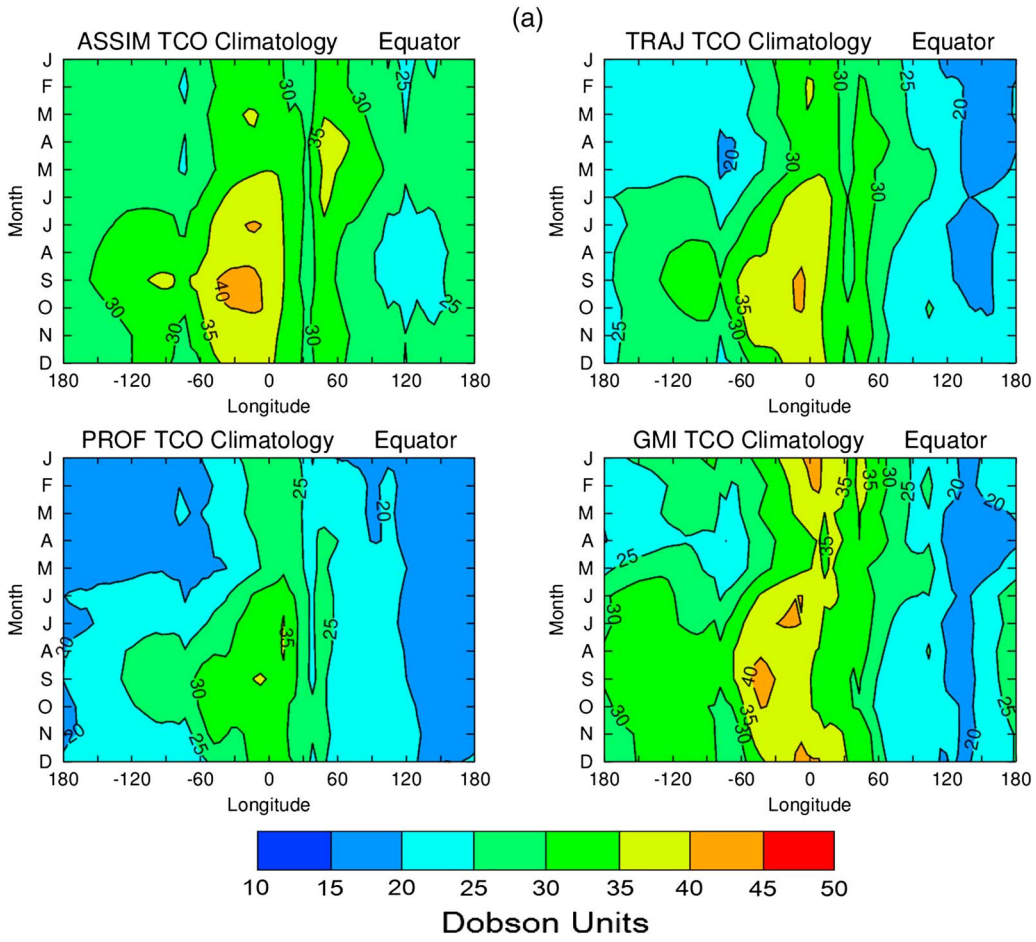

Figure 12. (a) Hovmoller plots of month versus longitude monthly TCO climatologies of the three data products and GMI model along the equator. (b) Same as Figure 12a but instead for SCO. All column amounts are in Dobson units. Measured offsets from the ozonesonde comparisons were applied here to TCO for plotting as in Figures 8–11 but not for SCO.

were chosen informally from cross-correlation calculations between TCO and the Niño 3.4 ENSO index time series to yield best overall correspondence between the two ENSO indices.) A monthly time series is then generated by taking the difference of western minus eastern Pacific TCO. This time series is then deseasonalized, followed by a 3 month running average (to be consistent with calculation of the monthly Niño 3.4 ENSO index). Because of very small zonal variability of monthly mean SCO of about 1–2 DU in the tropics [e.g., *Ziemke et al*., 2010, and references therein], the OEI time series derived from TCO is essentially the same as derived using total column ozone instead.

Figure 14a plots the TCO OEI derived separately from ASSIM (dotted purple curve), PROF (dashed blue curve), TRAJ (dotted-dashed green curve), and the CTM (solid red curve). Also included in Figure 14 is the Niño 3.4 index (solid black curve) and correlation "*r*" between Niño 3.4 and the four OEIs. All four OEIs extend from January 2005 through December 2012 except for PROF OEI which ends December 2008.

The four OEI time series in Figure 14a are nearly identical, differing by 1 DU or less each month. However, all four OEIs differ from Niño 3.4 at certain times of the record. It can be shown from daily values that these discrepancies between the OEIs and Niño 3.4 are generated by intraseasonal/Madden-Julian Oscillation (MJO) 1–2 month variability in tropical winds and temperatures [*Madden and Julian*, 1971, 1994, and references therein] affecting the OEI time series, especially during NH winter-spring months. An obvious discrepancy between the OEIs and Niño 3.4 index occurs around January 2008 (i.e., during La Niña) and shows all four OEIs with relative maxima while Niño 3.4 has a relative minimum.

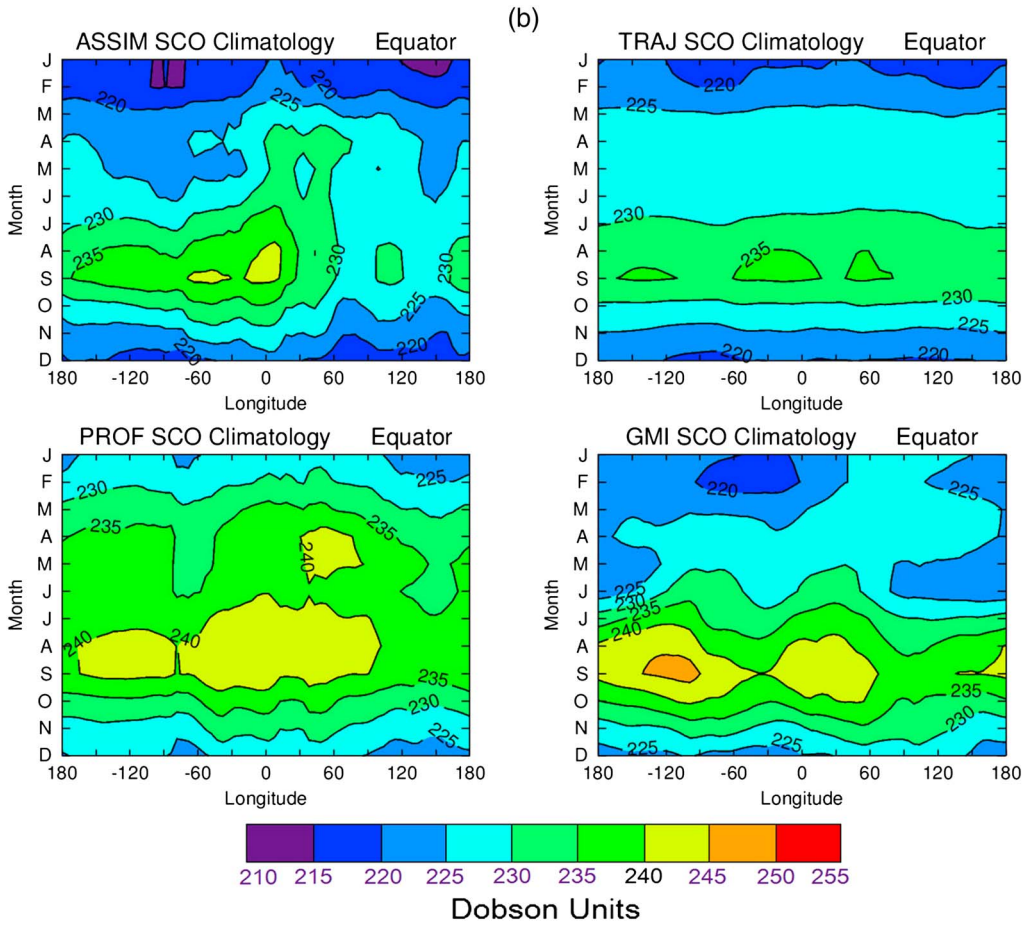

Figure 12. (continued)

All of the products including CTM show that this discrepancy between ENSO indices is caused by opposite phases of interannual and intraseasonal variability in tropospheric ozone (figures not shown). Understanding the tropical intraseasonal variability/MJO and its coupling effect with ENSO and monthly OEI is beyond the scope of our current study.

Table 1. Spatial Correlations Between Product TCO and Mean Field TCO Within Four Latitude Bands Beginning With Northernmost at the Top[a]

Product	Latitudes	DJF	MAM	JJA	SON
ASSIM	30°N–60°N	0.92	0.93	0.91	0.95
TRAJ	30°N–60°N	0.77	0.94	0.97	0.93
PROF	30°N–60°N	0.81	0.95	0.96	0.96
ASSIM	0–30°N	0.94	0.97	0.97	0.93
TRAJ	0–30°N	0.96	0.99	0.98	0.97
PROF	0–30°N	0.96	0.99	0.97	0.97
ASSIM	0–30°S	0.94	0.93	0.97	0.97
TRAJ	0–30°S	0.98	0.98	0.93	0.97
PROF	0–30°S	0.97	0.94	0.93	0.95
ASSIM	30°S–60°S	0.99	0.98	0.93	0.99
TRAJ	30°S–60°S	0.99	0.92	0.65	0.93
PROF	30°S–60°S	0.99	0.98	0.92	0.98

[a]Calculations are done for 3 month seasons of December–February, March–May, June–August, and September–November (DJF, MAM, JJA, and SON, respectively). Each latitude band is composed of 432 latitude-longitude grid points at 5° × 5° resolution.

Table 2. Similar to Table 1 but Instead for Product TCO Minus Mean Field TCO Differences (in Dobson Units) Rather Than Correlations

Product	Latitudes	DJF	MAM	JJA	SON
ASSIM	30°N–60°N	−3.10	−2.74	−2.85	−5.15
TRAJ	30°N–60°N	−8.53	−7.32	−6.68	−8.33
PROF	30°N–60°N	1.73	3.19	1.63	1.72
ASSIM	0–30°N	−2.48	−1.48	−0.37	−1.66
TRAJ	0–30°N	−7.93	−7.04	−6.52	−6.66
PROF	0–30°N	−1.96	−1.92	−1.63	−1.83
ASSIM	0–30°S	−0.58	−0.88	−2.15	−1.92
TRAJ	0–30°S	−6.88	−7.13	−8.22	−6.92
PROF	0–30°S	−1.58	−2.15	−1.27	0.22
ASSIM	30°S–60°S	−0.17	−1.25	0.00	−0.81
TRAJ	30°S–60°S	−6.63	−7.15	−7.03	−6.77
PROF	30°S–60°S	−0.46	0.19	0.47	1.83

We show that the profile ozone from ASSIM may provide some further insight regarding the vertical ozone profile contributions to the OEI in tropospheric ozone. In Figure 14b ASSIM upper tropospheric column ozone (dotted blue curve) is plotted with lower tropospheric column ozone (dashed red curve) and Niño 3.4 (solid black curve). Upper and lower tropospheric column ozone in Figure 14b are defined as the ozone column between 500 hPa to tropopause and 500 hPa to ground, respectively. The ASSIM ozone in Figure 14b indicates that most contribution to the OEI originates in the upper troposphere above 500 hPa. The month-by-month changes (temporal tendencies) in upper and lower tropospheric ozone generally track each other over the long record, but there are exceptions. One exception is centered about January 2010 (El Niño) and another about January 2011 (La Niña) where relative maxima for upper and lower tropospheric ozone are clearly not in phase. The ASSIM tropospheric profile ozone for these two cases suggests that upper and lower tropospheric ozone in the tropical Pacific is not always coherent; that is, an increase or decrease in the upper troposphere does not coincide with similar increase or decrease in the lower troposphere. This behavior seems to contradict the general in-phase response between upper and lower tropospheric ozone during ENSO events [*Oman et al.*, 2013]. Conclusions regarding ASSIM tropospheric ozone profile information are not certain due largely to reduced OMI efficiency in the low troposphere.

7.3. A Global Analysis of Interannual Variability of Ozone

General characteristics of interannual variability in global tropospheric and stratospheric ozone are examined using the 8 years of column ozone and profile ozone products. Figure 15 shows monthly zonal mean SCO (Figure 15a) and TCO (Figure 15b) from data assimilation. Both SCO and TCO in Figure 15 have recurring seasonal patterns each year but with some years indicating interannual change.

Table 3. Similar to Table 1 but Instead for RMS Differences of Product TCO Minus Mean Field TCO (in Dobson Units) Rather Than Correlations[a]

Product	Latitudes	DJF	MAM	JJA	SON
ASSIM	30°N–60°N	1.23	1.52	2.00	1.26
TRAJ	30°N–60°N	2.22	1.52	1.13	1.35
PROF	30°N–60°N	3.04	1.46	1.38	1.08
ASSIM	0–30°N	1.82	2.19	1.70	2.07
TRAJ	0–30°N	1.32	1.10	1.16	1.24
PROF	0–30°N	1.54	1.77	1.56	1.33
ASSIM	0–30°S	1.73	1.53	1.18	1.74
TRAJ	0–30°S	0.97	0.95	1.84	1.74
PROF	0–30°S	1.34	1.58	2.48	3.01
ASSIM	30°S–60°S	0.77	0.62	0.93	0.79
TRAJ	30°S–60°S	0.86	1.18	2.11	1.75
PROF	30°S–60°S	0.98	0.64	1.72	2.05

[a]All TCO averages were removed prior to calculation of these RMS numbers.

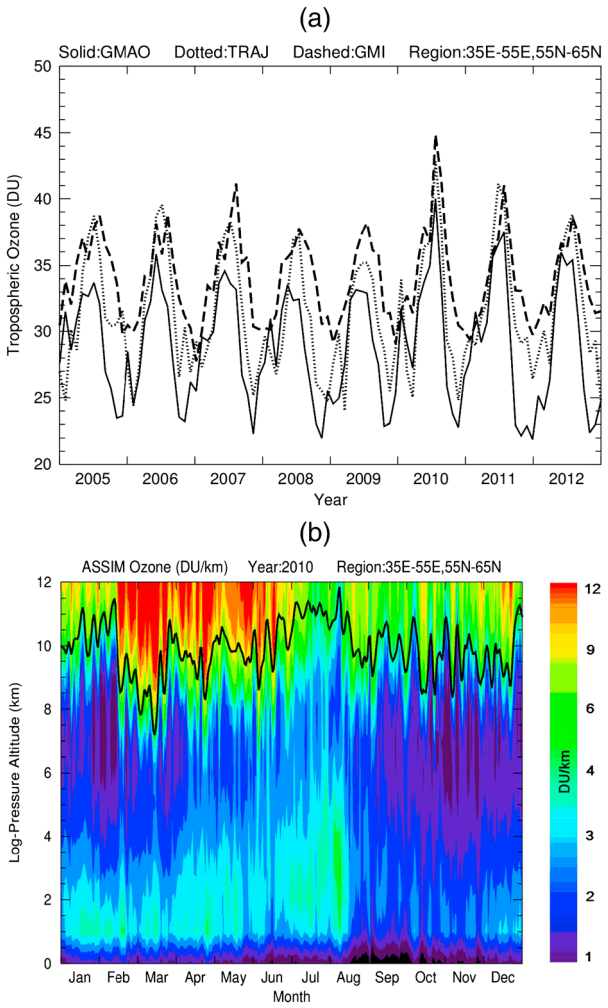

Figure 13. (a) Monthly mean TCO time series measurements averaged over Western Russia from ASSIM (solid), TRAJ (dotted), and GMI model (long dashed). TCO for the three products was averaged over the region 35°E–55°E, 55°N–65°N. Anomalous increases in TCO over the region occurred in July 2010 for all three TCO time series in conjunction with record dry conditions involving high tropospheric temperatures and uncontrolled wildfires. (b) Contour plot of daily ozone profiles (calculated vertical concentrations in DU km^{-1}) from ASSIM for year 2010 over the same broad region. The thick black curve is NCEP tropopause pressure in log-pressure altitude.

For SCO there is a 2–3 year QBO cycle in the tropics and extratropics and also anomalous enhanced SCO in the tropics and subtropics around the months October 2010–January 2011. Equatorial TCO for the final 2–3 years is slightly larger compared to the previous years.

The interannual features in SCO and TCO are better identified by removing seasonal cycles in the data. The SCO and TCO from ASSIM in Figure 15 were deseasonalized and replotted in Figure 16a to better identify interannual differences and near-decadal changes. For comparison with ASSIM, deseasonalized SCO and TCO from TRAJ measurements are shown in Figure 16b. The SCO and TCO products from ASSIM and TRAJ in Figure 16 are equivalent everywhere to within a few Dobson units. Figure 16 shows that both SCO products have a clear QBO in the tropics and throughout the SH, but in the NH the QBO signal for SCO is mixed with other interannual changes occurring in middle-high latitudes (discussed later).

It can be shown for all data products including the CTM that even though interannual changes of TCO on a regional basis may constitute many DUs, interannual changes for zonal mean TCO are exceedingly small. Figure 16 shows that interannual variability of zonal mean TCO is only about 1–2 DU on average for ASSIM and TRAJ. This shows that most all interannual changes present in zonal mean total column ozone are due to interannual change in SCO. Both zonal mean TCO products in Figure 16 also show

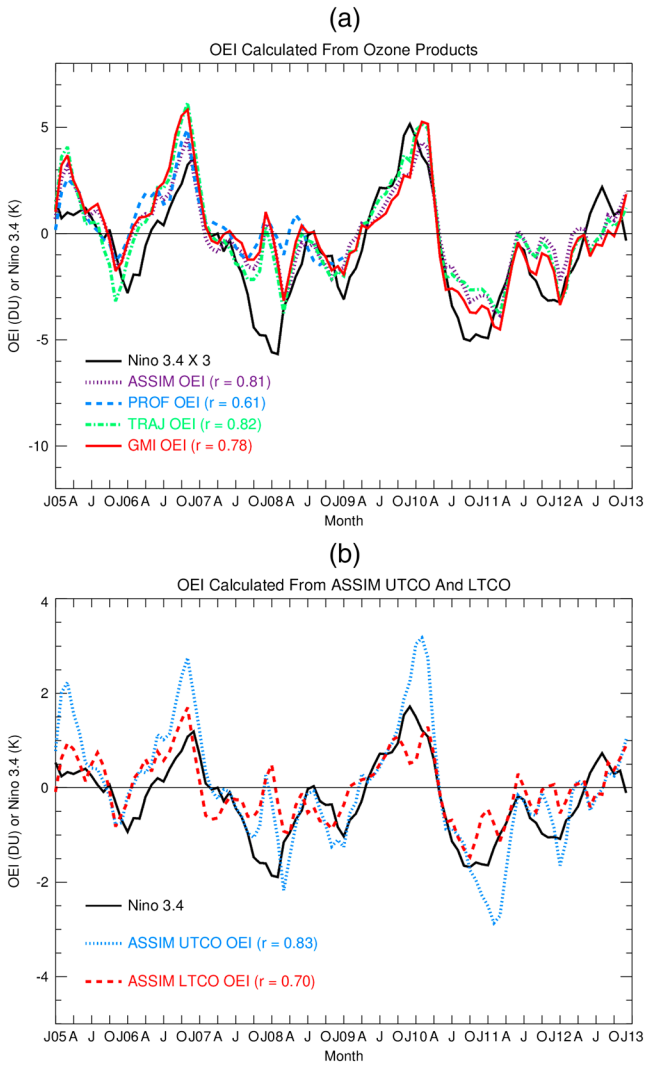

Figure 14. (a) Monthly tropospheric ozone ENSO Index (OEI) derived separately from ASSIM (dotted purple curve), PROF (dashed blue curve), TRAJ (dash-dotted green curve), and GMI CTM (solid red curve). Also shown is the Niño 3.4 monthly temperature anomaly ENSO index (solid black curve) along with listed time series correlations "*r*" between the Niño 3.4 index and OEIs from the three products and CTM. OEI time series are given in Dobson units, while the Niño 3.4 units are in Kelvin. All four OEIs extend from January 2005 through December 2012 except for PROF OEI which ends December 2008. (b) ASSIM upper tropospheric column ozone (UTCO, dotted blue curve) is plotted with lower tropospheric column ozone (LTCO, dashed red curve) and Niño 3.4 (solid black curve). Upper and lower tropospheric column ozone are defined as the ozone column from 500 hPa to tropopause and 500 hPa to ground, respectively.

small increases in the latter years of the record. This is currently being investigated using the CTM (figures not shown) which also shows small net increase in TCO in the latter years during predominantly La Niña conditions. *Doherty et al*. [2006] indicated from a coupled chemistry climate model that the shift from El Niño to La Niña conditions in the troposphere may produce several percent increase in the global tropospheric ozone burden. This is not inconsistent with the small net increases we find in tropical tropospheric ozone in Figure 16.

In Figures 17–20 we show interannual variability of zonal mean ozone for selected latitude bands in correspondence to the 8 year record of column ozone in Figure 16. In Figure 17 deseasonalized ozone profiles (in DU km^{-1}) from ASSIM (Figure 17a) are plotted with ozone profiles from MLS (Figure 17b) for general one-to-one comparison. Largest contribution to the equatorial QBO shown earlier in Figure 16 lies within the vertical band of about 20–25 km in log-pressure altitude in Figure 17.

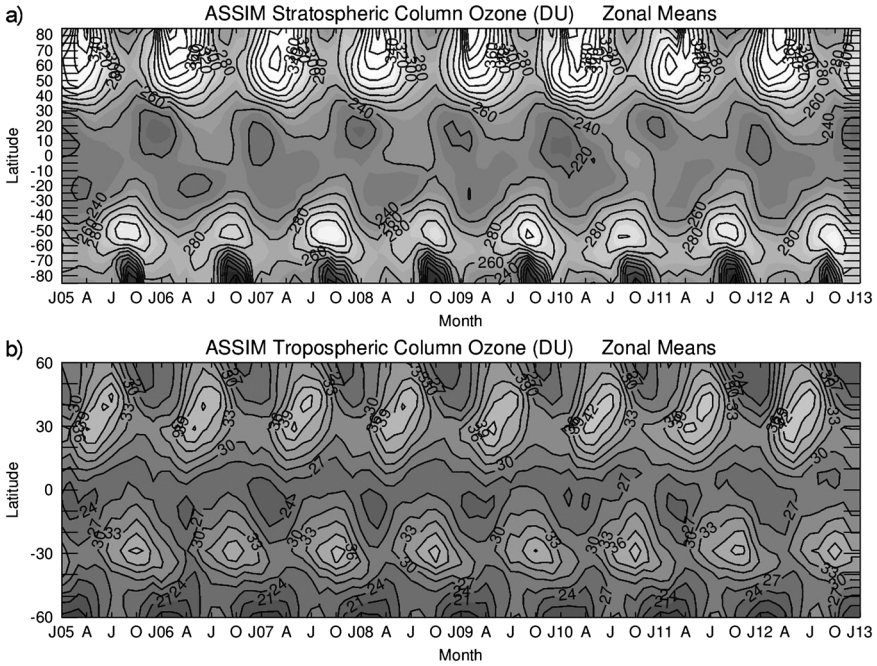

Figure 15. (a) Monthly zonal mean SCO in Dobson units for 2005–2012 from the data assimilation product. (b) Same as Figure 15a but instead for TCO. Dark to light shading in each panel designates smaller to higher column amounts, respectively. The contour values for Figure 15a (Figure 15b) increments by 20 (3) Dobson units.

As stated earlier in section 5, TCO for the CTM seemed to be as good as any of the three products when based on the ozonesonde comparisons. The CTM performs exceptionally well in simulating TCO, but there remain problems in simulating trace gases including ozone in the stratosphere, particularly the tropical lower stratosphere. This problem originates from spurious transport of ozone caused by errors in the analyzed winds [*Tan et al*., 2004]. Although *Tan et al*. [2004] diagnosed an older assimilation system, comparisons of MLS ozone and N_2O with our CTM simulations using MERRA meteorology show that spurious transport in the tropical and subtropical lower stratosphere is still a problem. Our 1-1 comparisons between Singapore and MERRA monthly zonal winds as a function of pressure in the tropical lower stratosphere (not shown) indicate substantial phase shifts between them of several months in the QBO signals. This error in MERRA winds produces an error in the QBO signal in stratospheric ozone simulated by the CTM. This error is demonstrated in Figure 18 by plotting equatorial deseasonalized zonal mean SCO for ASSIM (solid black curve), TRAJ (dotted blue), and CTM (solid red). The CTM in Figure 18 has a large phase lag of many months relative to measurements for the first two QBO cycles. The basic reason for the shift of the QBO signal for the CTM is that ASSIM and TRAJ both use MLS profile ozone and reproduce the QBO in these ozone measurements regardless of even moderate errors in winds. In contrast, the CTM does not include MLS ozone and is directly sensitive to errors in the 3-D wind fields.

Figure 19 is similar to Figure 17 but instead shows ASSIM ozone profile densities for both 40°N (Figure 19a) and 40°S (Figure 19b). Ozone profiles in the SH at 40°S in Figure 19b have a clear 2–3 year QBO signal (which is mostly out of phase with the equatorial QBO signal), but not so for the NH because of other additional interannual changes. Most stratospheric ozone interannual variability in both the NH and SH midlatitudes lies around 20 km. ASSIM deseasonalized ozone profiles are plotted again in Figure 20 as in the previous figure but instead for high polar latitudes 80°N (Figure 20a) and 80°S (Figure 20b). Largest interannual variability at 80°N in Figure 20a occurs during winter when OMI has no ozone measurements because of polar night. Several enhanced interannual changes in ozone in Figure 20a associated with sudden stratospheric warming events occur in the northern polar region. These NH warming events are identified as large interannual changes during winter-spring months. Two intense stratospheric warming events in the NH during winter months are identified in 2006 and 2009.

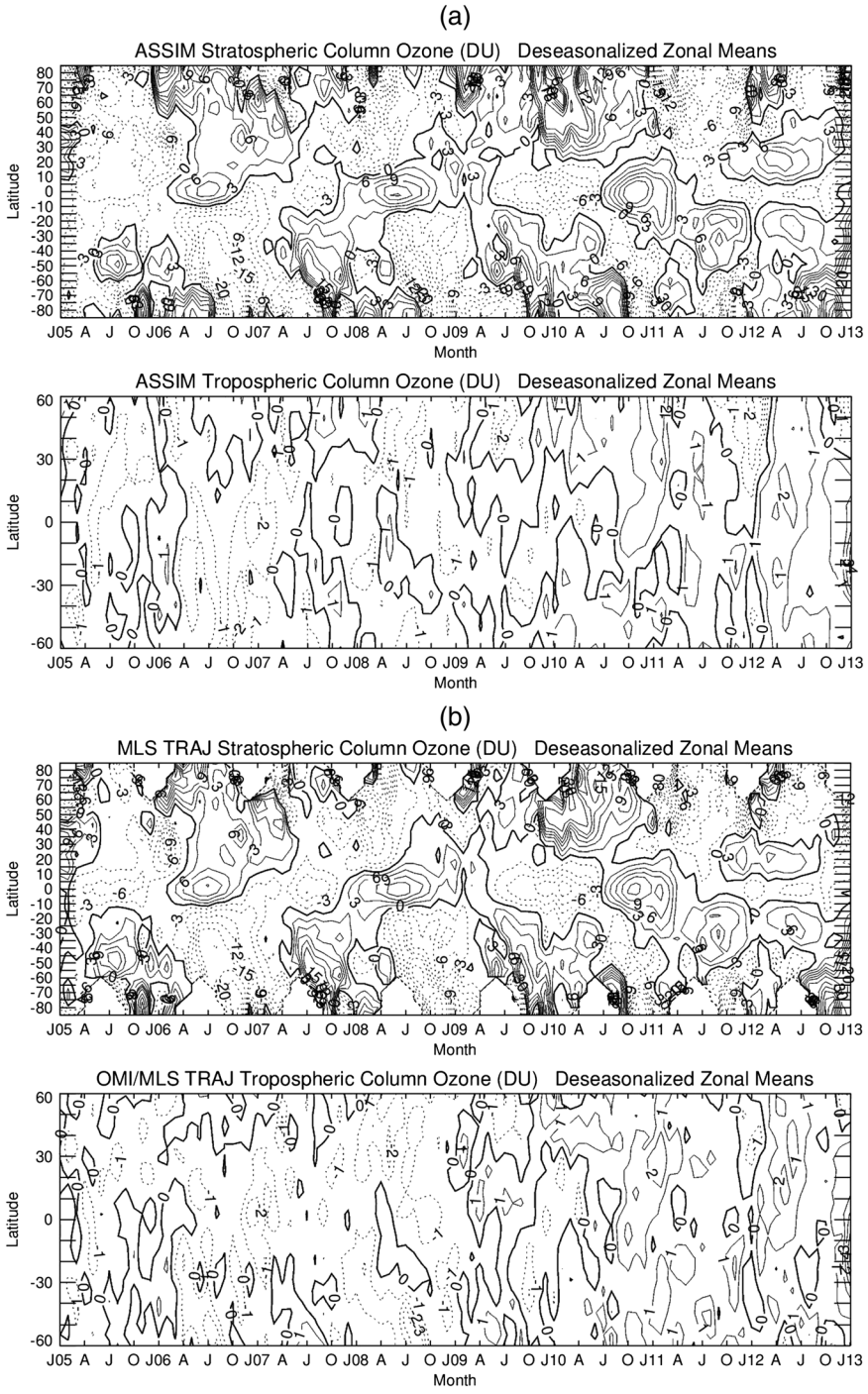

Figure 16. (a) Contour diagrams of the same ozone data plotted in Figure 15 but with all measurements deseasonalized. The contour increments for Figure 16a (Figure 16b) is 3 (1) Dobson units. (b) Same as Figure 16a but instead for TRAJ SCO and TCO measurements.

At least three stratospheric warmings in Figure 20a coincide with Arctic split events [e.g., *Ripesi et al.*, 2012] in spring 2005, winter 2009, and winter 2010. For each split event the ASSIM ozone has a relative minimum in the vertical centered around 15 km. These relative minima in the lower stratosphere are not present for other warming events such as 2006 and 2011. As a note, winter-spring 2011 in Figure 20a indicates reductions of ozone rather than increases in the lower stratosphere. The anomalous reduction

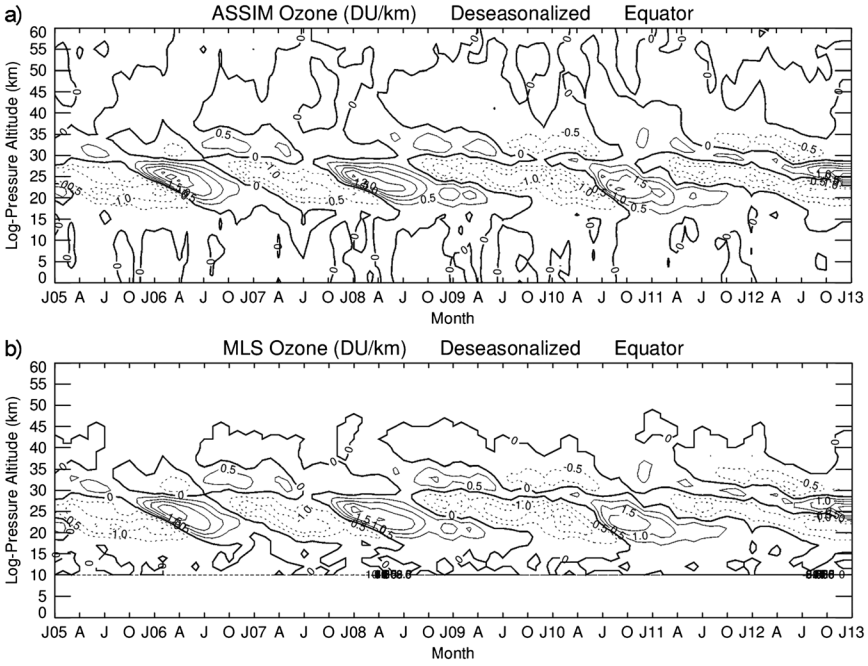

Figure 17. (a) Equatorial ozone concentration (in units DU km^{-1}) from the deseasonalized data assimilation product plotted as log-pressure altitude (in units km) versus month. These ozone concentrations were derived from monthly means by interpolating the product log-pressure surface ozone measurements to pressure levels $1013.25 \cdot \exp(-z/7)$ where z is log-pressure altitude in units kilometers and the pressure is in units hectopascal. (b) Same as Figure 17a but for MLS ozone profiles.

of stratospheric ozone in March 2011 was largely explained in recent studies by *Manney et al.* [2011], *Isaksen et al.* [2012], and *Strahan et al.* [2013] as an unusually strong polar vortex that year which suppressed and delayed the transport of stratospheric ozone from lower latitudes. Interannual variability in the SH polar region in Figure 20b is small when compared to the NH polar region. For the SH, two anomalous events (exceeding +5 DU km^{-1}) occurred in the range 20–25 km during October–November in 2005 and 2012. These two events signify anomalously high stratospheric ozone levels in the immediate lower stratosphere polar region during Antarctic ozone depletion conditions.

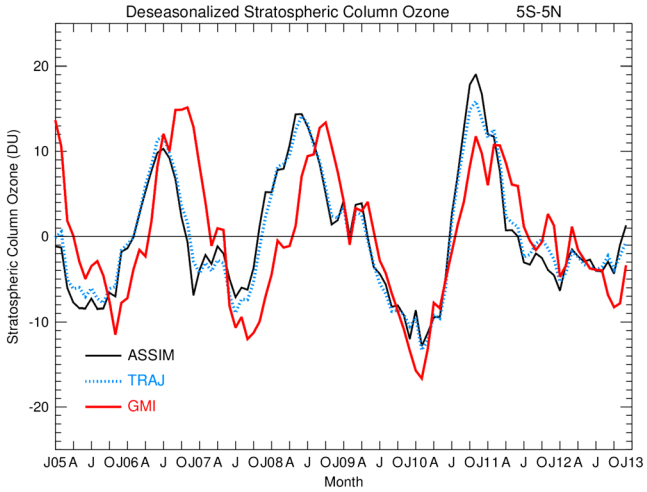

Figure 18. Deseasonalized zonally averaged monthly mean stratospheric column ozone (in Dobson units) averaged about the equator (5°S–5°N) for ASSIM (black solid curve), TRAJ (blue dotted curve), and the GMI model (red solid curve).

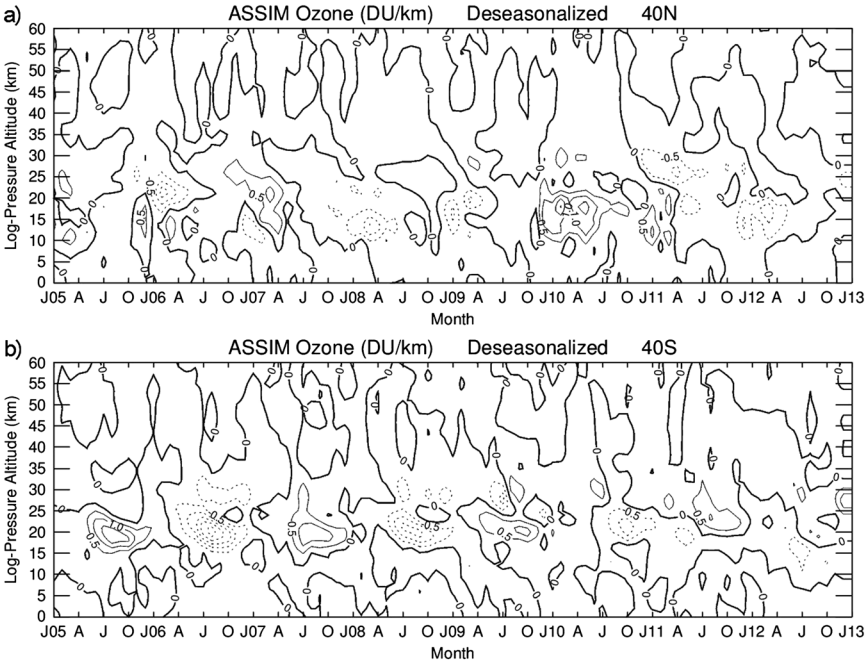

Figure 19. (a) Same as Figure 17 for ASSIM ozone but instead at latitude 40°N. (b) Same as Figure 17 for ASSIM ozone but instead at latitude 40°S.

8. Summary

Three different strategies to obtain tropospheric and stratospheric ozone from Aura OMI/MLS measurements beginning late 2004 have been evaluated for their overall data quality and usefulness for science applications. These three strategies are trajectory mapping (denoted TRAJ), direct profile retrieval (denoted

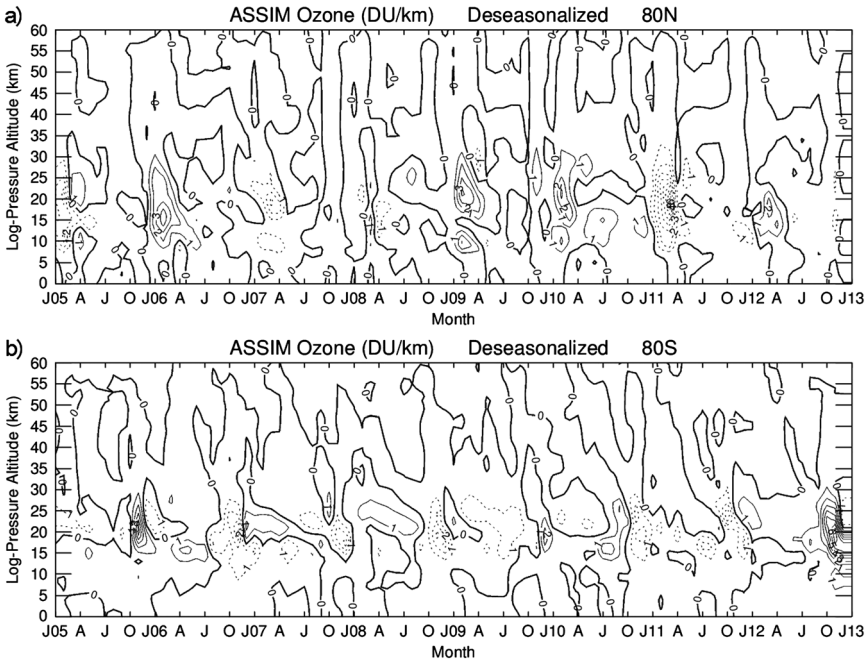

Figure 20. (a) Same as Figure 17 for ASSIM ozone but instead at latitude 80°N. (b) Same as Figure 17 for ASSIM ozone but instead at latitude 80°S.

PROF), and data assimilation (denoted ASSIM). The evaluation of the three products includes validation using ozonesondes and comparisons with the GMI CTM.

The three OMI/MLS ozone data products were compared with ozonesonde measurements from WOUDC, SHADOZ, and NDACC. The TRAJ tropospheric column ozone (TCO) product was shown to have the largest bias (i.e., a low bias exceeding 5 DU on average) relative to the sondes. This low bias appears as a manifestation of MLS ozone being high biased in the low stratosphere [e.g. *Livesey et al*., 2011] and an unresolved relative calibration offset existing between OMI v8.5 and MLS v3.3 measurements. The ASSIM TCO also has a low bias, but it is reduced by better accounting for measurement uncertainties/noise that also reduces RMS values with sondes. The RMS numbers are smallest, and the correlations are closest to being one for the ASSIM ozone. The assimilation method uses three-dimensional variational assimilation and thereby reduces the offsets and RMS differences with sondes.

The daily ozone products are demonstrated to be useful for evaluating regional case studies such as the 2010 Russian wildfires and the 2008 Beijing Olympics. In summer 2010 intense wildfires persisted in Western Russia caused by anomalously dry conditions. Tropospheric ozone was largest in all of the products and the CTM during July 2010 compared to any other month of the 2005–2012 record. The anomalous increase in tropospheric ozone in Western Russia was about 5 DU compared to an average background of around 35 DU. Tropospheric ozone profiles from data assimilation indicate that the anomalous increases in tropospheric ozone in July 2010 extended deep throughout the troposphere with most contribution coming from below 500 hPa. The ozone increases coincided with anomalous meteorological conditions that year involving an unusual stationary high-pressure blocking event and warm temperatures.

The photochemical production of tropospheric ozone is sensitive to the concentrations of NO_x and volatile organic compounds, UV radiation, and meteorological conditions. Drastic changes in ozone precursors may not necessarily coincide with measureable changes in tropospheric ozone. A case study example of this effect was the 2008 Beijing Olympics whereby there were large reductions in regional pollution including ozone precursors, yet OMI/MLS data products and the CTM all showed no reduction in tropospheric ozone.

With the Aura OMI and MLS measurements beginning late 2004, the ozone product records are now long enough to study and characterize interannual to near-decadal variability of stratospheric and tropospheric ozone. The OMI/MLS ozone products show that while the quasi-biennial oscillation (QBO) is the dominant source of interannual variability of stratospheric ozone in the tropics and SH, variability of stratospheric ozone in the NH includes an additional mix of anomalous interannual increases and decreases. During the Aura record there were several events of stratospheric sudden warmings in the NH including split events. These sudden warmings occur in polar latitudes around winter months when there are no OMI ozone measurements due to polar night. MLS stratospheric ozone profiles also do not fully cover the polar region and do not "fill in" the ozone profiles missing between orbit paths as assimilation does.

It is well known that the El Niño–Southern Oscillation (ENSO) is the dominant source of interannual change in tropospheric ozone in the tropical Pacific. The tropospheric ozone ENSO index (OEI) of *Ziemke et al*. [2010] was calculated for the three data products and the CTM for the 8 year Aura record. OEI derived for the three products and CTM are all remarkably consistent to within about 1 DU of each other every month. Ozone profiles from data assimilation suggest further that the OEI is driven mostly by ENSO-forced ozone variations in the upper troposphere above 500 hPa.

The three ozone data products and the CTM show that zonal mean tropospheric column ozone has only small interannual changes of about 1–2 DU in any latitude range. The data products and CTM also show a slight increase of 2–4 DU in tropospheric ozone toward the last 3 years of measurements in our study (i.e., years 2010–2012); the CTM suggests that this may be due in part to La Niña conditions persisting in the tropics toward the end of the Aura record (this is ongoing work beyond our current study).

When based on the ozonesonde validation and science applications investigated, the ASSIM ozone is overall the most useful of the three OMI/MLS data products. The assimilated ozone provides a continuous global record of ozone which includes profile information. Profile information for ozone is not provided by the TRAJ product, and the PROF profile product has a shorter record (through 2008) and comparatively coarse vertical resolution for ozone profiles. Despite lack of profile information, there are benefits of using the TRAJ daily ozone product. The TRAJ product provides a long record of ozone and includes additional geophysical parameters

within the product files such as in situ cloud fractions and cloud pressures, tropopause pressures (various definitions), and tropospheric and stratospheric column amounts (using various tropopause pressure definitions). The GMAO assimilated ozone in our study is currently a preliminary product that will at later time be made available to the public following further validation by K. Wargan et al. (manuscript in preparation, 2013). Information about using the TRAJ product can be obtained from the NASA Goddard ozone air quality website http://ozoneaq.gsfc.nasa.gov/.

Acknowledgments
The authors thank the Aura MLS and OMI instrument and algorithm teams for the extensive satellite measurements used in this study. We also thank the Editor and three reviewers for valuable comments that were very beneficial in improving the paper. OMI is a Dutch-Finnish contribution to the Aura mission. Funding for this research was provided in part by NASA NNH07ZDA001N-AST.

References

Chandra, S., J. R. Ziemke, W. Min, and W. G. Read (1998), Effects of 1997–1998 El Niño on tropospheric ozone and water vapor, *Geophys. Res. Lett.*, *25*, 3867–3870, doi:10.1029/98GL02695.

Chandra, S., J. R. Ziemke, P. K. Bhartia, and R. V. Martin (2002), Tropical tropospheric ozone: Implications for dynamics and biomass burning, *J. Geophys. Res.*, *107*(D14), 4188, doi:10.1029/2001JD00044.

Chandra, S., J. R. Ziemke, and R. V. Martin (2003), Tropospheric ozone at tropical and middle latitudes derived from TOMS/MLS residual: Comparison with a global model, *J. Geophys. Res.*, *108*(D9), 4291, doi:10.1029/2002JD002912.

Doherty, R. M., D. S. Stevenson, C. E. Johnson, W. J. Collins, and M. G. Sanderson (2006), Tropospheric ozone and El Niño–Southern Oscillation: Influence of atmospheric dynamics, biomass burning emissions, and future climate change, *J. Geophys. Res.*, *111*, D19304, doi:10.1029/2005JD006849.

Duncan, B. N., J. J. West, Y. Yoshida, A. M. Fiore, and J. R. Ziemke (2008), The influence of European pollution on ozone in the Near East and northern Africa, *Atmos. Chem. Phys.*, *8*, 22–2283.

Edwards, D. P., et al. (2003), Tropospheric ozone over the tropical Atlantic: A satellite perspective, *J. Geophys. Res.*, *108*(D8), 4237, doi:10.1029/2002JD002927.

Fishman, J., C. E. Watson, J. C. Larsen, and J. A. Logan (1990), Distribution of tropospheric ozone determined from satellite data, *J. Geophys. Res.*, *95*, 3599–3617, doi:10.1029/JD095iD04p03599.

Fishman, J., A. E. Wozniak, and J. K. Creilson (2003), Global distribution of tropospheric ozone from satellite measurements using the empirically corrected tropospheric ozone residual technique: Identification of the regional aspects of air pollution, *Atmos. Chem. Phys.*, *3*, 893–907, doi:10.5194/acp-3-893-2003.

Fishman, J., J. K. Creilson, A. E. Wozniak, and P. J. Crutzen (2005), Interannual variability of stratospheric and tropospheric ozone determined from satellite measurements, *J. Geophys. Res.*, *110*, D20306, doi:10.1029/2005JD005868.

Hogg, R. V., and A. T. Craig (1978), *Introduction to Mathematical Statistics*, 4th ed., Macmillan, New York.

Hudson, R. D., and A. M. Thompson (1998), Tropical tropospheric ozone from total ozone mapping spectrometer by a modified residual method, *J. Geophys. Res.*, *103*, 22,129–22,145, doi:10.1029/98JD00729.

Isaksen, I. S. A., et al. (2012), Attribution of the arctic ozone column deficit in March 2011, *Geophys. Res. Lett.*, *39*, L24810, doi:10.1029/2012GL053876.

Kar, J., J. Fishman, J. K. Creilson, A. Richter, J. R. Ziemke, and S. Chandra (2010), Are there urban signatures in the tropospheric ozone column products derived from satellite measurements?, *Atmos. Chem. Phys.*, *10*, 5213–5222, doi:10.5194/acp-10-5213-2010.

Kim, J. H., M. J. Newchurch, and K. Han (2001), Distribution of tropical tropospheric ozone determined by the scan-angle method applied to TOMS measurements, *J. Atmos. Sci.*, *58*(18), 2699–2708, doi:10.1175/1520-0469(2001)058<2699:DOTTOD>2.0.CO;2.

Lee, S., D. M. Shelow, A. M. Thompson, and S. K. Miller (2010), QBO and ENSO variability in temperature and ozone from SHADOZ, 1998–2005, *J. Geophys. Res.*, *115*, D18105, doi:10.1029/2009JD013320.

Lelieveld, J., and F. J. Dentener (2000), What controls tropospheric ozone?, *J. Geophys. Res.*, *105*(D3), 3531–3551, doi:10.1029/1999JD901011.

Liu, X., P. K. Bhartia, K. Chance, R. J. D. Spurr, and T. P. Kurosu (2010a), Ozone profile retrievals from the Ozone Monitoring Instrument, *Atmos. Chem. Phys.*, *10*, 2521–2537.

Liu, X., P. K. Bhartia, K. Chance, L. Froidevaux, R. J. D. Spurr, and T. P. Kurosu (2010b), Validation of Ozone Monitoring Instrument (OMI) ozone profiles and stratospheric ozone columns with Microwave Limb Sounder (MLS) measurements, *Atmos. Chem. Phys.*, *10*, 2539–2549.

Livesey, N. J., et al. (2011), EOS MLS Version 3.3 Level 2 data quality and description document, *Tech. Rep.*, Jet Propulsion Laboratory. [Available at http://mls.jpl.nasa.gov/.]

Madden, R. A., and P. R. Julian (1971), Description of the 40–50 day oscillation in the zonal wind in the tropical Pacific, *J. Atmos. Sci.*, *28*, 702–708.

Madden, R. A., and P. R. Julian (1994), Observations of the 40–50 day tropical oscillation—A review, *Mon. Weather Rev.*, *122*, 814–837.

Manney, G. L., et al. (2011), Unprecedented arctic ozone loss in 2011, *Nature*, *478*, 469–475, doi:10.1038/nature10556.

Martin, R. V., D. J. Jacob, R. M. Yantosca, M. Chin, and P. Ginoux (2003), Global and regional decreases in tropospheric oxidants from photochemical effects of aerosols, *J. Geophys. Res.*, *108*(D3), 4097, doi:10.1029/2002JD002622.

McPeters, R. D., G. J. Labow, and J. A. Logan (2007), Ozone climatological profiles for satellite retrieval algorithms, *J. Geophys. Res.*, *112*, D05308, doi:10.1029/2005JD006823.

McPeters, R. D., M. Kroon, G. Laboe, E. Brinksma, D. Balis, I. Petropavlovskikh, J. P. Veefkind, P. K. Bhartia, and P. F. Levelt (2008), Validation of the Aura Ozone Monitoring Instrument total column ozone product, *J. Geophys. Res.*, *113*, D15S14, doi:10.1029/2007JD008802.

Molod, A., L. Takacs, M. Suarez, J. Bacmeister, I.-S. Song, and A. Eichmann (2012), The GEOS-5 Atmospheric General Circulation Model: Mean Climate and Development from MERRA to Fortuna, NASA Technical Report Series on Global Modeling and Data Assimilation, NASA TM-2012-104606, vol. 28, 117 pp. [Available at http://gmao.gsfc.nasa.gov/pubs/tm/archive/tm_2012.php.]

Moxim, W. J., and H. Levy II (2000), A model analysis of tropical South Atlantic Ocean tropospheric ozone maximum: The interaction of transport and chemistry, *J. Geophys. Res.*, *105*, 17,393–17,415, doi:10.1029/2000JD900175.

Newchurch, M. J., X. Liu, and J. H. Kim (2001), Lower-tropospheric ozone (LTO) derived from TOMS near mountainous regions, *J. Geophys. Res.*, *106*, 20,403–20,412, doi:10.1029/2000JD000162.

Oman, L. D., A. R. Douglass, J. R. Ziemke, J. M. Rodriguez, D. W. Waugh, and J. E. Nielsen (2013), The ozone response to ENSO in Aura satellite measurements and a chemistry-climate simulation, *J. Geophys. Res. Atmos.*, *118*, 965–976, doi:10.1029/2012JD018546.

Purser, R. J., W.-S. Wu, D. F. Parrish, and N. M. Roberts (2003a), Numerical aspects of the application of recursive filters to variational statistical analysis. Part I: Spatially homogeneous and isotropic Gaussian covariances, *Mon. Weather Rev.*, *131*, 1524–1535.

Purser, R. J., W.-S. Wu, D. F. Parrish, and N. M. Roberts (2003b), Numerical aspects of the application of recursive filters to variational statistical analysis. Part II: Spatially inhomogeneous and anisotropic general covariances, *Mon. Weather Rev.*, *131*, 1536–1548.

Rienecker, M. M., et al. (2011), MERRA—NASA's Modern-Era Retrospective Analysis for Research and Applications, *J. Clim.*, *24*, 3624–3648, doi:10.1175/JCLI-D-11-00015.1.

Ripesi, P., F. Ciciulla, F. Maimone, and V. Pelino (2012), The February 2010 Arctic Oscillation Index and its stratospheric connection, *Q. J. R. Meteorol. Soc.*, *138*, 1961–1969, doi:10.1002/qj.1935.

Sauvage, B., R. V. Martin, A. van Donkelaar, and J. R. Ziemke (2007), Quantification of the factors controlling tropical tropospheric ozone and the South Atlantic maximum, *J. Geophys. Res.*, *112*, D11309, doi:10.1029/2006JD008008.

Schoeberl, M. R., et al. (2007), A trajectory-based estimate of the tropospheric ozone column using the residual method, *J. Geophys. Res.*, *112*, D24S49, doi:10.1029/2007JD008773.

Stajner, I., et al. (2008), Assimilated ozone from EOS-Aura: Evaluation of the tropopause region and tropospheric columns, *J. Geophys. Res.*, *113*, D16S32, doi:10.1029/2007JD008863.

Strahan, S. E., B. N. Duncan, and P. Hoor (2007), Observationally-derived diagnostics of transport in the lowermost stratosphere and their application to the GMI chemistry transport model, *Atmos. Chem. Phys.*, *7*, 2435–2445.

Strahan, S. E., A. R. Douglass, and P. A. Newman (2013), The contributions of chemistry and transport to low arctic ozone in March 2011 derived from Aura MLS observations, *J. Geophys. Res. Atmos.*, *118*, 1563–1576, doi:10.1002/jgrd.50181.

Sudo, K., and M. Takahashi (2001), Simulation of tropospheric ozone changes during 1997–1998 El Niño: Meteorological impact on tropospheric photochemistry, *Geophys. Res. Lett.*, *23*, 4091–4094, doi:10.1029/2001GL13335.

Tan, W. W., M. A. Geller, S. Pawson, and A. da Silva (2004), A case study of excessive subtropical transport in the stratosphere of a data assimilation system, *J. Geophys. Res.*, *109*, D11102, doi:10.1029/2003JD004057.

Thompson, A. M., J. C. Witte, R. D. Hudson, H. Guo, J. R. Herman, and M. Fujiwara (2001), Tropical tropospheric ozone and biomass burning, *Science*, *291*, 2128–2182.

Thompson, A. M., et al. (2003), Southern Hemisphere Additional Ozonesondes (SHADOZ) 1998–2000 tropical ozone climatology 2. Tropospheric variability and the zonal wave-one, *J. Geophys. Res.*, *108*(D2), 8241, doi:10.1029/2002JD002241.

Trenberth, K. E. (1997), The definition of El Niño, *Bull. Am. Meteorol. Soc.*, *78*(12), 2771–2777, doi:10.1175/1520-0477(1997)078<2771:TDOENO>2.0.CO;2.

Van der Werf, G. R., J. T. Randerson, L. Giglio, G. J. Collatz, P. S. Kasibhatla, and A. F. Arellano (2006), Interannual variability in global biomass burning emissions from 1997 to 2004, *Atmos. Chem. Phys.*, *6*, 3423–3441.

Vasilkov, A., J. Joiner, R. Spurr, P. K. Bhartia, P. Levelt, and G. Stephens (2008), Evaluation of the OMI cloud pressures derived from rotational Raman scattering by comparisons with other satellite data and radiative transfer simulations, *J. Geophys. Res.*, *113*, D15S19, doi:10.1029/2007JD008689.

Wang, Y. H., D. J. Jacob, and J. A. Logan (1998), Global simulation of tropospheric O3-Nox-hydrocarbon chemistry 1. Model formulation, *J. Geophys. Res.*, *103*, 10,713–10,725, doi:10.1029/98JD00158.

Witte, J. C., M. R. Schoeberl, A. R. Douglass, J. F. Gleason, N. A. Krotkov, J. C. Gille, K. E. Pickering, and N. Livesey (2009), Satellite observations of changes in air quality during the 2008 Beijing Olympics and Paralympics, *Geophys. Res. Lett.*, *36*, L17803, doi:10.1029/2009GL039236.

Witte, J. C., A. R. Douglass, A. da Silva, O. Torres, R. Levy, and B. N. Duncan (2011), NASA A-Train and Terra observations of the 2010 Russian wildfires, *Atmos. Chem. Phys.*, *11*, 9287–9301, doi:10.5194/acp-11-9287-2011.

Wozniak, A. E., J. Fishman, P.-H. Wang, and J. K. Creilson (2005), Distribution of stratospheric column ozone (SCO) determined from satellite observations: Validation of solar backscattered ultraviolet (SBUV) measurements in support of the tropospheric ozone residual (TOR) method, *J. Geophys. Res.*, *110*, D20305, doi:10.1029/2005JD005842.

Wu, W.-S., R. J. Purser, and D. F. Parrish (2002), Three-dimensional variational analysis with spatially inhomogeneous covariances, *Mon. Weather Rev.*, *130*, 2905–2916.

Yan, H., L. Chen, J. Tao, L. Su, J. Huang, D. Han, and C. Yu (2012), Corrections for OMI SO2 BRD retrievals influenced by row anomalies, *Atmos. Meas. Tech.*, *5*, 2635–2646, doi:10.5194/amt-5-2635-2012.

Ziemke, J. R., S. Chandra, and P. K. Bhartia (1998), Two new methods for deriving tropospheric column ozone from TOMS measurements: The assimilated UARS MLS/HALOE and convective-cloud differential techniques, *J. Geophys. Res.*, *103*, 22,115–22,127, doi:10.1029/98JD01567.

Ziemke, J. R., and S. Chandra (1999), Seasonal and interannual variabilities in tropical tropospheric ozone, *J. Geophys. Res.*, *104*, 21,425–21,442, doi:10.1029/1999JD900277.

Ziemke, J. R., S. Chandra, B. N. Duncan, L. Froidevaux, P. K. Bhartia, P. F. Levelt, and J. W. Waters (2006), Tropospheric ozone determined from Aura OMI and MLS: Evaluation of measurements and comparison with the Global Modeling Initiative's Chemical Transport Model, *J. Geophys. Res.*, *111*, D19303, doi:10.1029/2006JD007089.

Ziemke, J. R., S. Chandra, B. N. Duncan, M. R. Schoeberl, M. R. Damon, O. Torres, and P. K. Bhartia (2009), Recent biomass burning events in the tropics and elevated concentrations of tropospheric ozone, *Geophys. Res. Lett.*, *36*, L15819, doi:10.1029/2009GL039303.

Ziemke, J. R., S. Chandra, L. D. Oman, and P. K. Bhartia (2010), A new ENSO index derived from satellite measurements of column ozone, *Atmos. Chem. Phys.*, *10*, 3711–3721.

Ziemke, J. R., S. Chandra, G. J. Labow, P. K. Bhartia, L. Froidevaux, and J. C. Witte (2011), A global climatology of tropospheric and stratospheric ozone derived from Aura OMI and MLS measurements, *Atmos. Chem. Phys.*, *11*, 9237–9251, doi:10.5194/acp-11-9237-2011.